




# A comprehensive quantitative characterisation of the multiphase microstructure of a thick-section high strength steel

Virgínia Bertolo<sup>1,\*</sup> , Quanxin Jiang<sup>1</sup>, Sebastian Scholl<sup>2</sup>, Roumen H. Petrov<sup>1,3</sup>, Ude Hangen<sup>4</sup>, Carey Walters<sup>5,6</sup>, Jilt Sietsma<sup>1</sup>, and Vera Popovich<sup>1</sup>

<sup>1</sup>Department of Materials Science and Engineering, Delft University of Technology, Mekelweg 2, 2628 CD Delft, The Netherlands

<sup>2</sup>Aktien-Gesellschaft der Dillinger Hüttenwerke, Werkstraße 1, 66763 Dillingen, Germany

<sup>3</sup>Department of Electromechanical, Systems and Metals Engineering, Ghent University, Technologiepark 131, 9052 Ghent, Belgium

<sup>4</sup>Bruker Nano Surfaces, Dennewartstrasse 25, 52068 Aachen, Germany

<sup>5</sup>Structural Dynamics, TNO, Leeghwaterstraat 44, 2628 CA Delft, The Netherlands

<sup>6</sup>Maritime and Transport Technology, Delft University of Technology, Mekelweg 2, 2628 CD Delft, The Netherlands

**Received:** 30 November 2021

**Accepted:** 20 March 2022

**Published online:**

30 March 2022

© The Author(s) 2022

## ABSTRACT

The through-thickness heterogeneous microstructure of thick-section high strength steels is responsible for the significant scatter of properties along the thickness. In this study, in order to identify the critical microstructural features in the fracture behaviour and allow for design optimisation and prediction of structural failure, the through-thickness microstructure of thick-section steels was extensively characterised and quantified. For this purpose, samples were extracted from the top quarter and middle thickness positions, and a combination of techniques including chemical composition analysis, dilatometry, and microscopy was used. The hardness variation through the thickness was analysed via micro-Vickers measurements and the local hardness variation in the middle section was studied via nanoindentation. The middle section presented larger prior austenite grain (PAG) sizes and larger sizes and area fraction of inclusions than the top section. Additionally, cubic inclusions were observed distributed as clusters in the middle, sometimes decorating PAG boundaries. Defects associated with the cubic inclusions or the interface between the matrix and the circular and cubic inclusions were observed in the mid-thickness. Moreover, the middle section presented long interfaces with the most significant hardness gradients due to the presence of hard centreline segregation bands. Hence, the microstructural and nanoindentation analyses indicated the middle section as the most likely area to have the lowest fracture toughness and, therefore, the most unfavourable section for fracture performance of the

Handling Editor: Sophie Primig.

Address correspondence to E-mail: v.moretebarbosabertolo@tudelft.nl

investigated S690QL high strength steel. The detrimental effect of the middle section was confirmed via CTOD tests where the middle presents lower fracture toughness than the top section.

## Introduction

The multiphase microstructure of high strength steels (HSSs), composed of multiple bcc micro-constituents, carbides and inclusions, is responsible for the attractive combination of strength and toughness, greatly valued for structural applications, such as components of highly loaded offshore lifting equipment. Supporting high loads is of utmost importance for these structures, and thick-section steel plates are required. The commonly found microstructural complexity of HSSs may become more pronounced when produced in thick sections due to the non-uniform cooling rates and deformation levels through the thickness experienced during the processing route (e.g. rolling and heat treatments such as quenching and tempering). As a result, different phases, grain sizes, inclusions, phase fractions, and the presence of elemental segregation may be observed from the outer surface of the steel plate towards its centre. Consequently, a considerable through-thickness variation of mechanical properties is observed [1–3]. Although HSSs display the desired properties for structural applications, harsh service conditions (e.g. temperature and loading levels) may make them prone to cleavage fracture leading the structure to fail catastrophically. Hence, to predict and control structural failure and optimise thick-section steel's design it is essential to accurately characterise the through-thickness microstructure and the resulting local variations of mechanical properties.

Several studies [1–5] have investigated the heterogeneous through-thickness microstructure and its effect on the mechanical properties of thick-section steel plates. However, the key microstructural features have not been thoroughly characterised and quantified for adequate experimental and modelling assessment of cleavage fracture. While macroscopic inhomogeneities of steels have been modelled at millimetre scale with bimodal methods in cleavage simulations [6, 7], the heterogeneous microstructures at a smaller scale have not been taken into account.

The micromechanism-driven modelling of cleavage fracture typically accounts for the probability of failure based on the local stress (and sometimes strain) field, which is referred to as the local approach [8, 9]. On the grain scale and lower scale, multi-barrier theory has been proposed to represent the micromechanism of cleavage in local approaches (e.g. [10–13]). The application of a multi-barrier theory requires the knowledge of the nucleating particle size distribution and the grain (packet) size distribution. Therefore, the required comprehensive assessment of the microstructural variation of thick-section HSSs that allows for identifying potential critical sites in fracture behaviour has not yet been performed.

However, correlating the microstructural heterogeneity and properties of HSSs requires extensive work due to the microstructural complexity of the steel plate analysed herein. For this purpose, different techniques and methods have to be used to obtain relevant microstructural information, making it possible to establish a clear processing-microstructure-properties relationship. Moreover, this study faces some challenges.

First, we face the difficulty to distinguish and quantify bcc micro-constituents. The microstructure of quenched and tempered HSSs consists of a mixture of tempered bcc micro-constituents such as martensite and bainite [1]. Due to the similar structure and morphology of these constituents, it is a significant challenge to distinguish and quantify them by standard microscopy techniques. Alternatively, dilatometry is a technique used in phase transformation studies and may be useful to distinguish and quantify phases formed under a given thermal cycle [14]. Furthermore, although all previously mentioned constituents are bcc-structured, the use of Electron Backscatter Diffraction (EBSD) can be valuable. Since each phase has its characteristics inherited from the phase transformation nature, their diffraction pattern may be different. Consequently, some parameters calculated from the EBSD data (e.g. image quality, kernel average misorientation, and grain orientation spread) can assist the characterisation and quantification of phases in a multi-bcc-phase microstructure.

For instance, several studies unanimously use EBSD to differentiate bcc micro-constituents in steels [15–17]. However, EBSD analysis may not lead to an accurate and conclusive analysis in bcc micro-constituents distinction, especially for tempered microstructures where the separation of martensite from other phases is difficult because the quality of the Kikuchi pattern is increasingly becoming more similar to the other phases [15, 17]. Another beneficial approach can be to perform the material characterisation in the reverse way where the local mechanical response of the bcc micro-constituents is used to distinguish them.

Recently, tests on the nanoscale allowed the measurement of properties of individual features. Chang et al. [18] observed that ferrite, bainite, and martensite have considerably different average nanohardness (3.8, 4.4, and 5.6 GPa, respectively) in a multiphase advanced high strength steel. This difference may assist their distinction along with other techniques. However, attention must be paid since the measurement scatter sometimes causes overlap between the results for several phases. Although this approach is promising to distinguish bcc micro-constituents, it may be challenging to apply it to tempered steels as the nanohardness values for the phases can become close and even overlap, making it difficult to distinguish between them [19].

Second, conventional microhardness measurement is insufficient to measure the local gradient of properties in detail due to its large indent size compared to the dimensions of microstructural features. Hence, investigation in the nanoscale is needed. Additionally, indentation hardness is useful for investigating the effects of microstructural heterogeneities on properties since it has a direct relationship with other mechanical properties (e.g. elastic moduli, strength, and ductility) [20, 21]. Moreover, hardness analysis may indicate critical sites in fracture behaviour that can affect the global material performance. For instance, Hidalgo, Celada-Casero and Santofimia [22] reported that the significant hardness difference between Mn enriched areas and the surrounding matrix was responsible for generating brittle fracture mechanisms in a medium Mn quenching and partitioning steel. Another observation regarding the effect of hardness gradients in fracture was done by Lee et al. [23], where large hardness variations make the material more prone to interfacial separation between matrix and hard particles, thus lowering the

fracture toughness [22, 23]. Hence, several studies reveal that hardness gradients may facilitate crack formation.

Therefore, this work aims to identify critical microstructural features for fracture in commercially available HSSs used in actual structures. Hence, the through-thickness microstructure of a commercially available thick-section quenched and tempered high strength steel is comprehensively investigated quantitatively. For this purpose, a combination of techniques involving chemical composition analysis, dilatometry, microscopy, and nanoindentation is used. The in-depth microstructural characterisation presented in this paper also represents a unique combination of microstructural parameters which are necessary for understanding and modelling the continuum-level properties. The effects of the multiphase and heterogeneous microstructure on mechanical properties and the identification of critical sites for fracture behaviour are investigated in terms of hardness and fracture toughness measurements. Moreover, nanoindentation was used to distinguish and quantify tempered bcc micro-constituents. This research will be useful to assess fracture behaviour, including the modelling approaches, and also to optimise steel design [24].

## Materials and methods

A commercially available 80 mm thick hot rolled, quenched and tempered S690 high strength steel plate (designated as S690QL in accordance with EN 10025-6 [25]) of  $80 \times 1500 \times 5000 \text{ mm}^3$ , used in offshore structural applications, with the limited toughness of the material as a critical factor, was studied. Out of the large commercial plate, smaller slabs ( $80 \times 740 \times 180 \text{ mm}$ ) were cut for further investigation. The chemical composition along the thickness of the S690QL steel plate was measured by LECO combustion analysis (for C, N, and S) and X-ray fluorescence (XRF) (for other elements) (Table 1). All elements, including the ones referred to as “other”, are in accordance with the range determined by the standard EN 10025-6 (max wt% of Mn = 1.7, Ni = 4.0, Cr = 1.5, Nb = 0.06, P = 0.02, N = 0.015, S = 0.01 and B = 0.005) [25]. In order to avoid any superficial layer that may affect the results, samples’ surfaces were ground with coarse P180 aluminium oxide sanding paper. Elements can

**Table 1** Through-thickness chemical composition of S690QL (measured by XRF and LECO)

wt (%)	Fe	C	Si	Al	Mo	Other
Top	Bal	0.170 ± 0.001	0.29 ± 0.02	0.070 ± 0.005	0.30 ± 0.01	Mn, Ni, Cr, Nb, P, N, S, B
Middle	Bal	0.160 ± 0.001	0.30 ± 0.03	0.08 ± 0.01	0.29 ± 0.02	

generally be considered homogeneously distributed through the plate thickness as average values are within the scatter except for C, which is higher in the top section.

To characterise the material along the thickness, samples were taken from the top quarter (further referred to as top) and middle thickness positions. The investigation of these thickness sections are motivated by (1) the quarter section is the thickness position required to be tested according to some standard and rules (e.g. 10025-6 [25]) for quality control of this type of steel, and (2) the middle section is reported as the most detrimental region for the performance of thick-section steel plates [1–4]. The bottom quarter section was also characterised and found to be identical to the top quarter sections. As isotropy is expected in this material, only one plane was chosen to be studied. Figure 1 schematically represents the investigated thickness positions and the RD × ND planes (hatched areas in top and middle thickness positions), in which 2-D characterisation and hardness analyses were carried out.

The through-thickness microstructure of the steel plate was etched with 5% Nital and analysed through conventional optical microscopy, optical Keyence digital microscopy, and scanning electron microscopy (SEM). The last two techniques mentioned were also used to quantify inclusions. The quantification of inclusions was performed according to ASTM E1245-03:2016 [26]. In order to reveal the Prior Austenite Grain (PAG) boundaries and, for the cases in which it is more interesting to have the centreline segregation bands more distinguishable from the matrix, samples were swabbed etched with a solution of 100 mL of saturated aqueous picric acid solution and 0.5 g of sodium dodecylbenzene sulfonate for 5 min.

Chemical composition measurements of centreline segregation bands in the middle section of the S690QL high strength steel plate were performed by Electron Probe Microanalysis (EPMA) with a JEOL JXA 8900R microprobe using an electron beam with

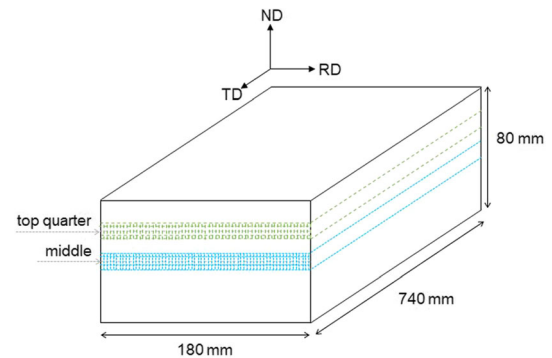


**Figure 1** Schematic illustration of the investigated thickness positions. The 2D analysis were carried out in the hatched RD × ND plane.

energy of 10 keV and beam current of 200 nA employing Wavelength Dispersive Spectrometry (WDS). Before EPMA measurements, the extremes of four segregation bands were identified by micro-indentations (HV 3) in an etched sample. Subsequently, the sample was polished again with 3 μm and 1 μm diamond solution and a colloidal silica solution (OPS). EPMA analysis was performed along a line of 300 μm in the thickness direction in increments of 2 μm. The line scan initiates and ends at points located outside the investigated segregation band, and both points are located approximately 150 μm from the centre of the band.

Dilatometry solid cylindrical specimens with dimensions of 10 mm × 4 mm (length × diameter) were placed in a Bähr 805A quench dilatometer (Bähr-Thermoanalyse GmbH, Germany), and induction heated and cooled using helium gas according to the industrial quenching thermal profile (Fig. 2). Note that for the middle section, a reduction in the cooling rate is observed from 200 °C. However, this reduction caused instrumental disturbances in the dilatometry curve. As no phase transformation below 200 °C is expected and was not observed for the top section, the cooling profile for the middle section has been simplified to 5 °C/s. Additionally, samples were analysed under a rapid quenching, 75 °C/s, to define the start and finish martensite transformation

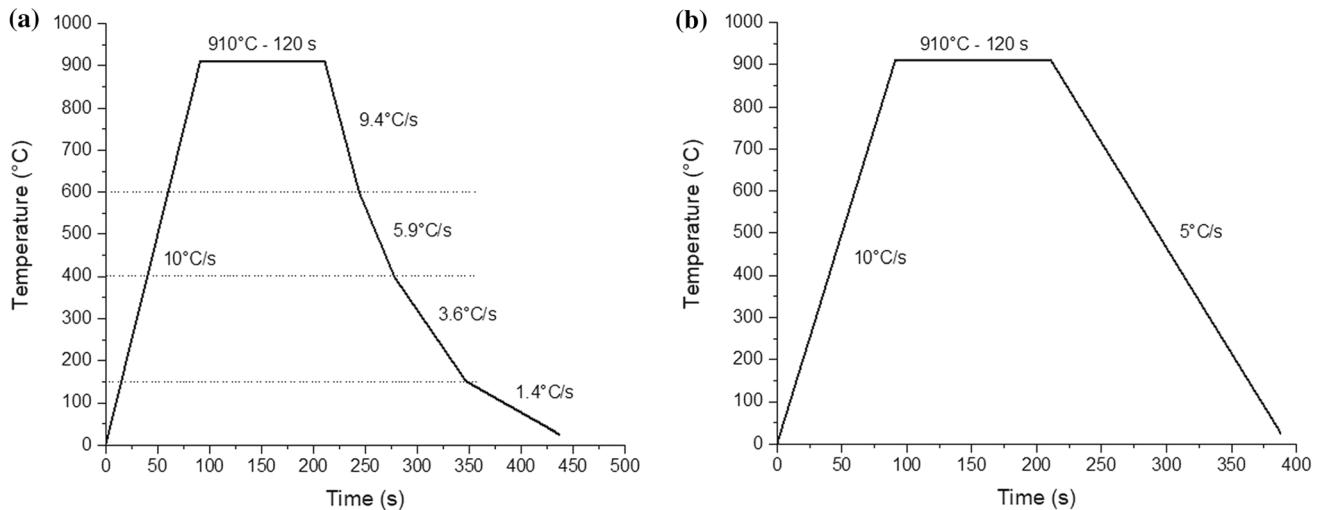


**Figure 2** Schematic representation of the thermal profile applied in the dilatometer to **a** top and **b** middle sections of the S690QL steel plate.

temperatures to be used as a reference. The temperature was monitored using a thermocouple spot-welded to the centre of the sample. Only the quenching stage was studied in the dilatometric tests since the tempering stage (between 600 and 650 °C for a few minutes) only affects the carbide precipitation and not the phase composition, if no retained austenite is present in the quenched material [27]. Consequently, no significant dilatometry signal can be expected. Afterwards, the results obtained by dilatometric tests are compared to theoretical CCT diagrams calculated by the JMatPro 7.0 software [28].

EBSD data were acquired on a JEOL scanning electron microscope equipped with a Field Emission Gun (FEG-SEM) using 25 kV accelerating voltage, the working distance of 25 mm, tilt angle of 70°, and step size 0.2  $\mu\text{m}$  by means of HKL Channel 5 software and post-processed with EDAX-TSL-OIM Analysis<sup>TM</sup> software. Scan areas around 360  $\mu\text{m}$   $\times$  270  $\mu\text{m}$  were randomly chosen from the top and middle sections (areas outside and including the segregation bands). Indentations (HV 3) were placed in the extremes of some segregation bands as previously explained to locate them. The initial EBSD post-processing step was the data clean-up. First, grain fit standardisation with grain tolerance angle of 5° and minimum grain size of 4 pixels was applied, considering that grains contain multiple pixel rows. Secondly, the neighbour orientation correlation procedure with a grain tolerance angle of 5° and a minimum confidence index of 0.1 was used. Lastly, neighbour phase correlation

with a minimum confidence index of 0.1 was applied. Afterwards, grains were defined with a tolerance angle of 5° and a minimum size of 4 pixels. Prior austenite grains were reconstructed in automatic mode using quadruplets as the reconstruction method, with tolerance for parent grain nucleation and growth equal to 3° and 6° by the ARPGE software developed by Cayron [29]. Each reconstructed map was post-processed in the TSL-OIM Analysis v7 software for grain size measurements. Minor and major axis (i.e. width and length, respectively) distributions of PAG were obtained using the TSL-OIM software, and the weighted average values were post-processed. PAG and packet sizes and block widths were measured according to ASTM E112-13 through the Heyn lineal intercept procedure [30].

The hardness analysis was carried out at micro- and nanoscales. Micro-Vickers hardness testing at the minimum load produces indents with a dimension of around 8  $\mu\text{m}$ , which are too large for most of the fine-scale features in the material. Although it would be possible to indent some particles and grains with dimensions larger than the minimum indent size, it would not be feasible to perform multiple indentations within individual features to obtain a representative result. Nevertheless, micro-Vickers hardness can still be used to evaluate the microstructure-hardness gradients through the thickness of the steel plate. Since the microstructure is significantly inhomogeneous and measurements in single features are not possible at the micro-scale,

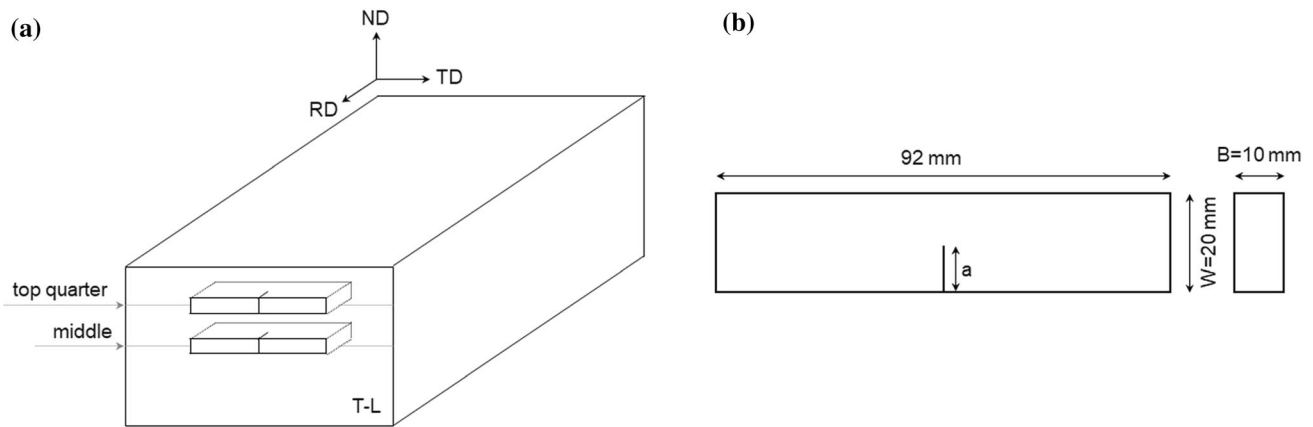


**Figure 3** Schematic illustration showing **a** the extraction of the SENB specimens from the steel plate in terms of thickness position and notch orientation to the RD, and **b** SENB specimen's

dimensions. ND is the normal direction, LD/RD are the longitudinal and rolling direction and TD the transverse direction.

hardness testing was performed through the thickness of the S690QL steel plate using a DuraScan 70 Emco with 30 N (indent size around 140  $\mu\text{m}$ ) to average out the local inhomogeneity and better understand how the bulk hardness varies in such thick quenched and tempered plates. Separate nanoindentation measurements were performed in a Hysitron TI 980 Triboindenter from Bruker (BNSM division, Aachen, Germany) in the accelerated property mapping (XPM) mode. A  $200 \times 200$  indentation map was made, covering an area of approximately  $320 \times 320 \mu\text{m}^2$  in the middle section of the S690QL steel plate. Shallow indents are performed to accommodate the high resolution. In this study, a preliminary analysis with different load levels and resultant indentation depths was made to identify the minimum load and depth in which the properties would become independent of the indentation depth to avoid indentation size effects (ISE) [31]. Therefore, the maximum load and resultant maximum indentation depth was defined as 1 mN and 70 nm. The indentations were made with a Berkovich indenter in load-controlled mode. In order to avoid overlapping of the indent's plastic zones, a distance of 1.6  $\mu\text{m}$  was kept between the indents. Hardness and reduced modulus properties were obtained from the load-displacement curves through the method of Oliver and Pharr [32]. Afterwards, EBSD scans using a step size of 0.07  $\mu\text{m}$  were performed in the tested area to correlate the obtained properties with microstructural aspects such as phases.

To investigate the through-thickness microstructural inhomogeneity effect on cleavage fracture, sub-

sized single edge-notched bending (SENB) specimens extracted from top and middle sections were tested by three-point bending similar to the ISO 12135 standard [33] at a deformation rate of 2 mm/s at  $-100 \text{ }^\circ\text{C}$  using a 350 kN MTS 858 servo hydraulic. The specimens are cooled down by immersion in liquid nitrogen until the heat exchange is over, approximately at  $-196 \text{ }^\circ\text{C}$  (liquid nitrogen's boiling temperature). This difference from the test temperature is to allow for thermal soaking and for more time to mount the sample in the set up. Afterwards, the specimens are placed in the machine, touching a thermal insulation material to avoid the fast heat exchange with the metallic parts. Then, when the test temperature is reached, the test is performed. The temperature applied in this work ( $-100 \text{ }^\circ\text{C}$ ) is to ensure that the test is performed in the brittle regime of the HSSs under study. The notch is oriented in T-L, parallel to the rolling direction, and the crack depth-width ratio ( $a/W$ ) is equal to 0.5. Details on specimen's dimensions and how they were extracted from the thick plate are given in Fig. 3.

## Results

### Through-thickness microstructural characterisation

The microscopic analysis of the as-received steel reveals a complex microstructure with different features interacting with each other. Figure 4 reasonably suggests that for both top and middle thickness

positions, grains resemble tempered micro-constituents, including martensite (TM)—grains with carbides oriented in multiple directions within individual laths; bainite (TB)—grains with carbides, from the original bainite grain, aligned in a single orientation within individual laths that are barely affected during tempering; and ferrite (F)—grains with no substructure [34]. However, it should be acknowledged that the distinction of these constituents is challenging due to their morphological similarity. Hence, this procedure is of limited accuracy. For this reason, other methods (e.g. dilatometry, EBSD and nanoindentation) to distinguish these bcc micro-constituents will be applied and discussed herein.

Dilatometry tests were performed for top and middle sections. Under the quenching and tempering processing route, steels mainly transform during quenching, while the tempering stage only causes carbide precipitation [27]. Thus, the investigated thickness sections were submitted to their respective quenching cooling routes to investigate the phase transformation that occur during the steel processing. The dilatometric curves and their derivatives are presented in Fig. 5. CCT diagrams for top and middle sections calculated with JMatPro software are shown in Fig. 6. This material's prior austenite grain size was observed to vary within a wide range, with its length between 5 and 70  $\mu\text{m}$ , approximately, with a mean intercept value around 20  $\mu\text{m}$  [3]. Hence, CCT curves for 5, 10, and 20  $\mu\text{m}$  grain sizes are presented. Further grain size analysis and discussion will follow later in this study.

The first deviation of the tangent from the dilatometric curves during cooling occurs in the temperature range of 480–490  $^{\circ}\text{C}$ , indicating the beginning of a phase transformation, followed by a significant expansion completed between 300 and 320  $^{\circ}\text{C}$ . The rapid quenching test performed by dilatometry indicates that the martensitic start and finish temperatures are around 415–430  $^{\circ}\text{C}$  and 165–185  $^{\circ}\text{C}$  (90% of martensite is formed at 255  $^{\circ}\text{C}$  calculated by the lever rule), respectively, for both positions in the thickness. These temperatures have a good agreement with the CCT diagrams (Fig. 6). Therefore, since the phase transformation under the cooling profile of the processing route begins and ends at temperatures above the start and finish martensitic temperatures, this transformation part likely results in another phase than martensite. According to the CCT diagrams, the most likely micro constituent formed in

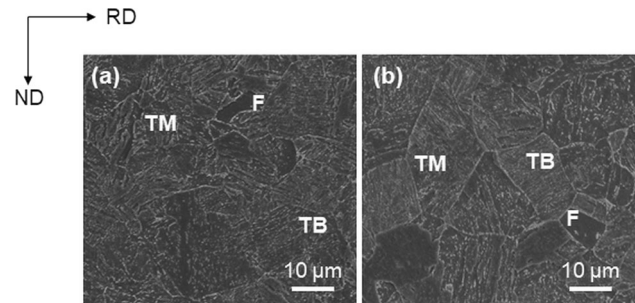


**Figure 4** Representative SEM micrographs of **a** top and **b** middle sections of the S690QL steel plate. Grains identified as F, TB, and TM refer to ferrite, tempered bainite, and tempered martensite, respectively.

this transformation temperature range is bainite. Figure 6 also shows that ferrite is prone to form under the quenching processing route depending on the prior austenite grain size. However, no significant dilatation was observed in the dilatometric curves that can be associated with ferrite formation.

Various inclusions are observed distributed through the matrix. Table 2 and Fig. 7 provide an overview of the most commonly found inclusions through the plate thickness. Most inclusions, regardless of the thickness position, have a complex chemical composition with mixtures of oxides, nitrides, sulphides, and carbonitrides.

The top and mid-thickness positions exhibit circular inclusions of similar sizes. However, larger cubic inclusions are observed in the middle, and they are present in larger area fractions than in the top. Furthermore, many of the inclusions in the middle section present important characteristics. Firstly, middle-section inclusions have often been seen associated with defects (e.g. voids and cracking of both matrix/inclusion interface and inclusion cracking) as shown in Fig. 7d–f. Secondly, cubic-shaped inclusions are often observed distributed as clusters. In some cases, these clusters are found decorating the PAG boundaries (Fig. 7e). Due to the proximity of the inclusions in the cluster, these inclusions may be viewed as a line of collinear inclusions, corresponding to a single large that can reach a length of up to 30  $\mu\text{m}$  (Fig. 7e, f).

Moreover, centreline segregation bands formed during the solidification process and pancaked during the hot rolling step were observed in the mid-thickness and are shown in Fig. 8a. The individually-identified centreline segregation bands exhibit widths in the range of 40 to 210  $\mu\text{m}$  that extend

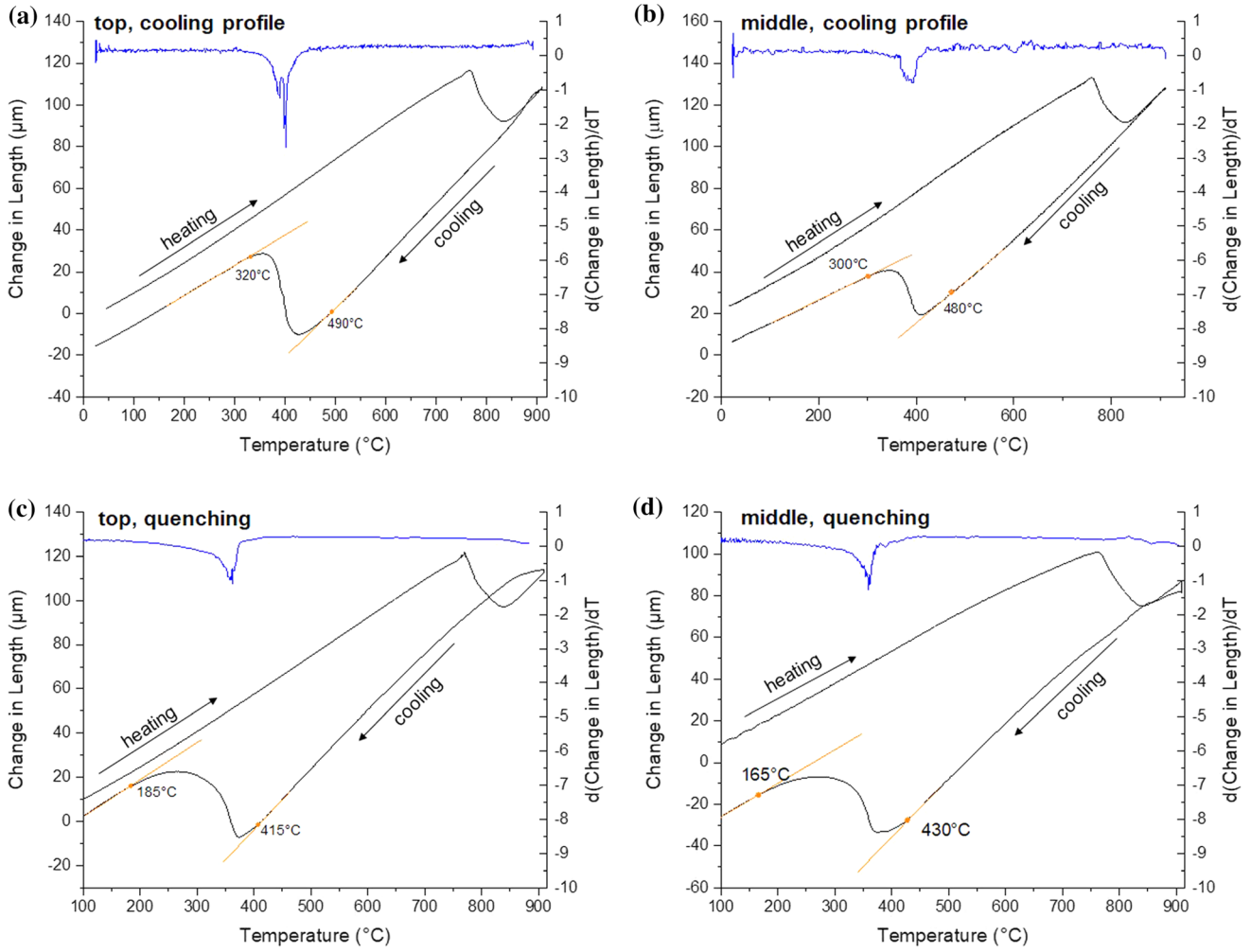


**Figure 5** Dilatometric and cooling differential curves of **a, c** top and **b, d** middle samples following the cooling profile of the quenching process of the S690QL steel processing route (**a, b**) and quenching (75 °C/s) (**c, d**), respectively.

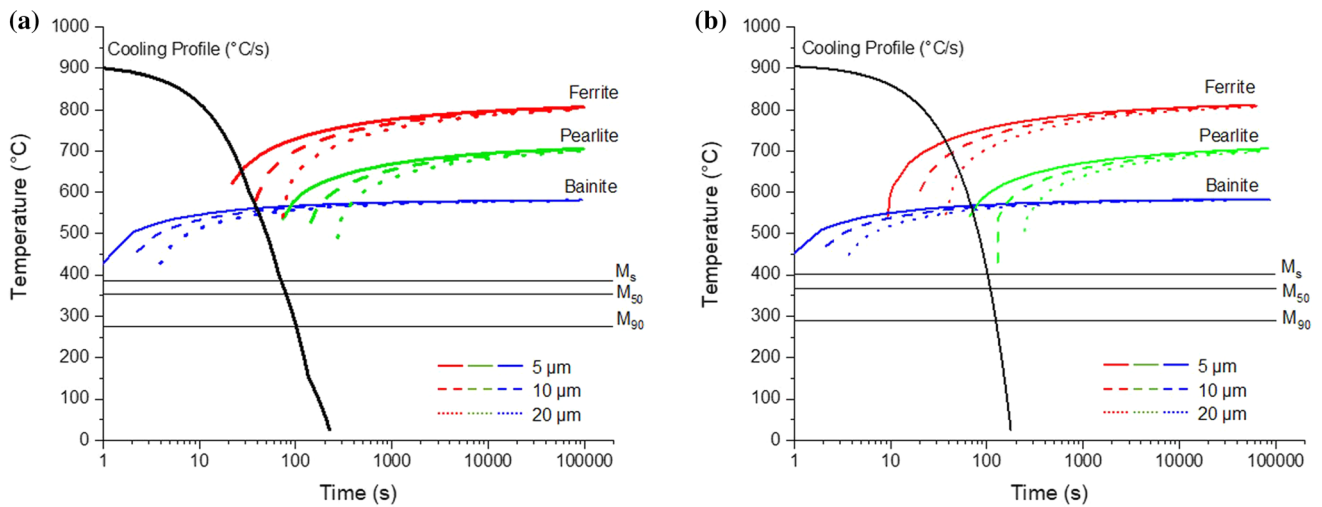


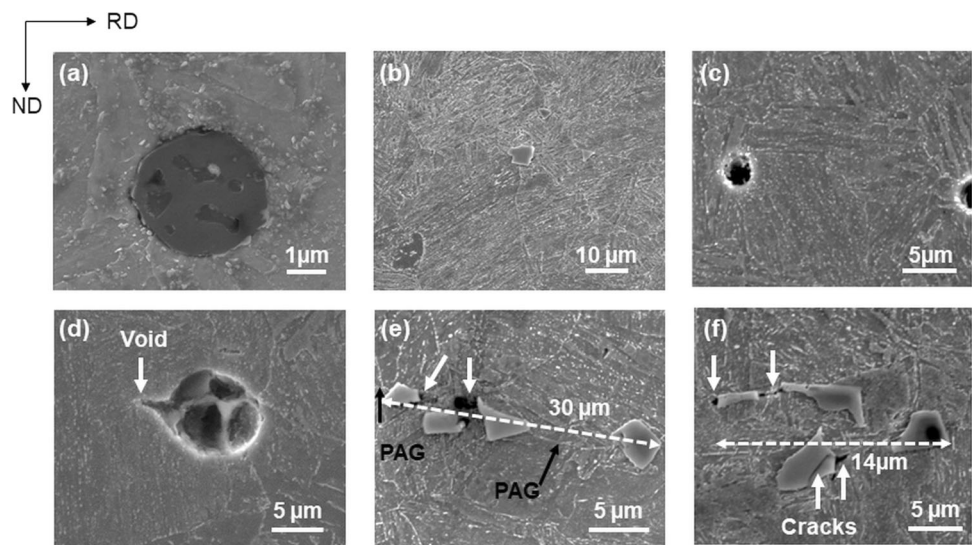
**Figure 6** CCT diagrams calculated with JMatPro software for **a** top and **b** middle sections of the S690QL steel plate showing ferritic, pearlitic, and bainitic starting temperatures for various prior austenite grain diameters from 5 to 20 μm.



**Table 2** Morphology, chemical composition, diameter, and area fraction of inclusions observed in the top and middle positions

Position	Type of inclusion	Composition	Diameter range (major axis), (μm)	Area fraction
Top	Circular	(Mg, Al, Ca)(O, N, S) (Mg, Al, Ca, Ti)(O, N)	1–5	$5 \times 10^{-4} \pm 3 \times 10^{-4}$
	Cubic	(B)(N)	1–2.5	$7 \times 10^{-5} \pm 4 \times 10^{-5}$
		(Nb, Ti)(C) (B, Ti, Nb)(N, C)	1–7	
Middle	Circular	(Mg, Al, Ca)(O) (Mg, Al, Ca, B)(N, S) (Mg, Al, Ca, Ti)(O, N)	1–5	$7 \times 10^{-4} \pm 3 \times 10^{-4}$
	Cubic	(Nb, Ti, Mg, Ca)(C, O, N) NbC (Nb, Ti)(C) (Nb, Ti)(C, N)	1–12	$2 \times 10^{-4} \pm 3 \times 10^{-5}$

**Figure 7** SEM micrographs of inclusions through the thickness of the S690QL steel plate showing **a** (Mg, Al, Ca)(O, N, S), **b** (Nb, Ti)(C) and (Nb, Ti)(C, N), and **c** (B)(N) inclusions for the top section; **d** (Mg, Al, Ca)(O, S), **e** (Nb, Ti)(C, N) and **f** NbC and (Nb, Ti)(N, C) inclusions for the middle section (Partially included in [3]).



approximately 8 mm across the thickness of the plate, thus being present in 10% of the material’s volume. As shown in Fig. 8c, clusters of Nb-rich cubic inclusions are directly associated with these segregation bands and aligned with them. It should be mentioned that in the top section, cubic Nb-rich inclusions are often observed distributed individually. However, they can also be scarcely seen distributed as clusters and aligned similarly to the segregation bands.

To characterise the chemical composition of segregation bands, EPMA line scan analyses were carried out from depleted through enriched areas. Elements including Mn, Cr, Mo, Si, Ni, and C were segregating in the bands. Figure 9 shows representative EPMA results for one of the analysed bands. The minimum and maximum elemental contents of

each element averaged over the various line scans are shown in Table 3.

C is the element that stands out most in the segregation bands in the middle section of the S690QL steel plate, followed by Mo, as shown in Table 3. The content of these elements in the enriched regions reaches levels up to 29 and 4.5 times, respectively, that of the low-solute regions. The other elements—Mn, Cr, Si, and Ni—despite being present in smaller proportions compared to C and Mo, still stand out for reaching up to twice the concentration measured in depleted areas. Note that the contents of these elements also vary within the segregation band. Such elemental variation in the mid-thickness are reported to affect phase transformation temperatures (e.g. bainite and martensite start temperature) and may

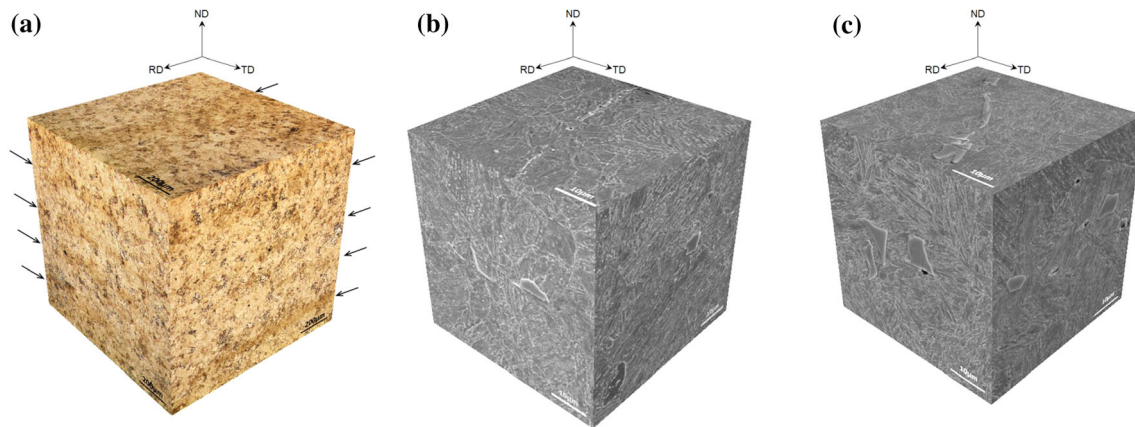


**Figure 8** 3D-representation of **a** pancaked centreline segregation bands in the middle section by optical microscopy, and clusters of cubic inclusions distributed aligned to the segregation bands

(indicated by black arrows) in the **b** top and **c** middle thickness positions of the S690QL steel plate by SEM. The scale bar in the SEM and optical images is 10  $\mu\text{m}$  and 200  $\mu\text{m}$ , respectively.

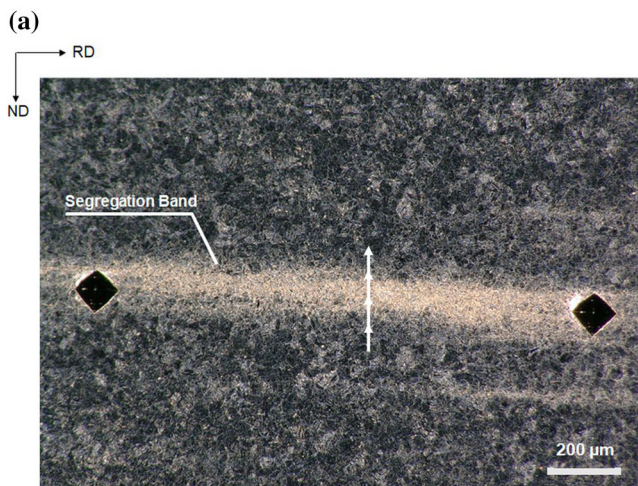
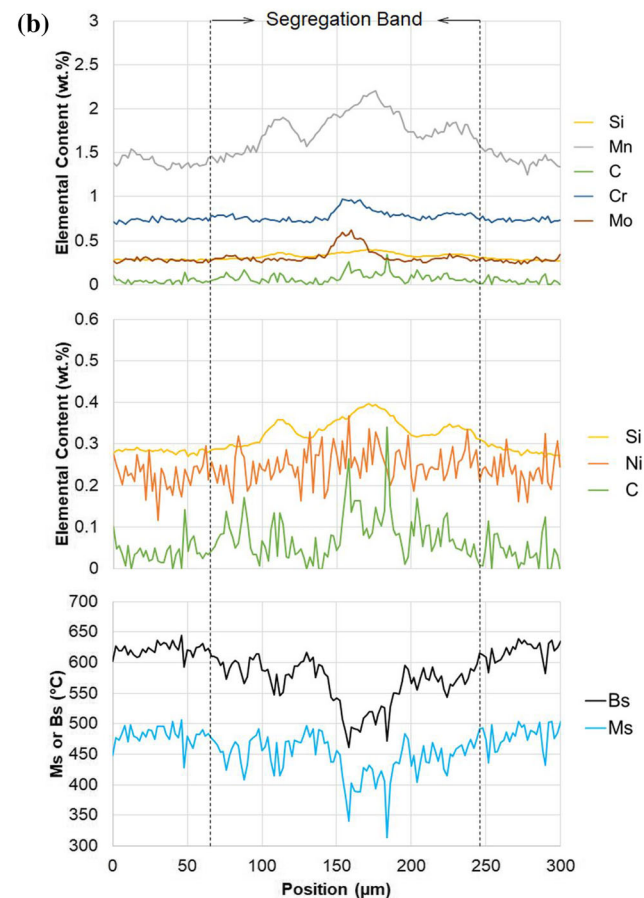


**Figure 9 a** Optical micrograph of the analysed segregation band. The white arrow shows the measurement start and end positions of the measurement as well as its direction. **b** Electron probe microanalysis results of the centreline segregation band. **c** Results



for C, Ni, and Si in another scale are presented in a separate chart to show their trends clearly. **d** Bainite and martensite starting temperature charts as a function of the composition (per distance) are also included.

**Table 3** Average maximum and minimum values for Mn, Cr, Mo, Si, Ni, and C elements along with EPMA line scan

Centreline segregation bands—elemental content (wt%)						
	Mn	Cr	Mo	Si	Ni	C
Max	2 ± 0.3	1.1 ± 0.2	0.8 ± 0.3	0.40 ± 0.04	0.35 ± 0.04	0.29 ± 0.04
Min	1.10 ± 0.10	0.70 ± 0.01	0.20 ± 0.01	0.30 ± 0.01	0.10 ± 0.02	0.01 ± 0.02

lead to different microstructural compositions in the centreline segregation bands compared to the depleted areas and also within the bands at the same cooling rate [35–37].

The compositional dependence of theoretical bainite and martensite start temperature ( $B_s$  and  $M_s$ ) is described by van Bohemen [38] and established by

$$B_s(^{\circ}C) = 839 - \sum_i P_i x_i - 270 \left[ 1 - e^{(-1.33x_C)} \right] \quad (1)$$

$$M_s(^{\circ}C) = 565 - \sum_i K_i x_i - 600 \left[ 1 - e^{(-0.96x_C)} \right] \quad (2)$$

where  $i = \text{Mn, Si, Cr, Ni, Mo}$ ;

$$\sum_i P_i x_i = 86x_{\text{Mn}} + 23x_{\text{Si}} + 67x_{\text{Cr}} + 33x_{\text{Ni}} + 75x_{\text{Mo}};$$

$$\sum_i K_i x_i = 31x_{\text{Mn}} + 13x_{\text{Si}} + 10x_{\text{Cr}} + 18x_{\text{Ni}} + 12x_{\text{Mo}}$$

and the concentration  $x_i$  is in wt%, and the subscript  $i$  indicates the element.

Calculations for  $B_s$  and  $M_s$  temperatures based on both equations were performed along with the EPMA line scan and are shown in Fig. 9c. According to the equations mentioned above, the higher the concentration of alloying elements, the lower the  $B_s$  and  $M_s$  temperatures. In the middle section of the steel plate under study, which presents an alternation of high-solute and low-solute bands, the difference between the highest and lowest  $B_s$  and  $M_s$  temperatures, considering all analysed segregation bands, can be up to 230 °C and 190 °C, respectively.

Visual inspection of prior austenite grains in the middle section (Fig. 10) suggests that this section presents a bimodal distribution of grains, with segregation bands featuring smaller grains than the areas outside these bands. The quantification of PAG and its substructure size is essential for establishing a microstructure-properties relationship and will be further presented along with the results obtained by the EBSD investigation.

The reconstructed PAGs, over the entire thickness of the steel plate, were found to have an elongated

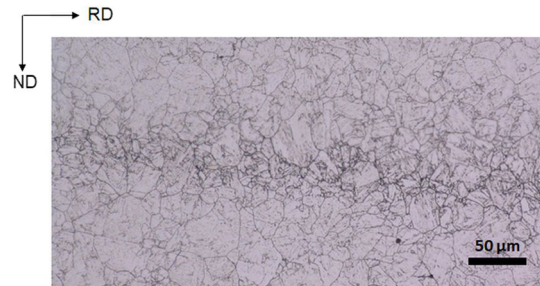


**Figure 10** Prior austenite grain (PAG) distribution in the middle of the plate with the segregation band showing a reduction in PAG size in the region of the band configuring a bimodal distribution of PAG.

shape (Fig. 11). The PAG aspect ratio was around 0.43 for all investigated areas (Fig. 12b). Hence, grain sizes are measured with respect to their width and length. Figure 12 displays the distribution and average values of PAG’s width and length. Table 4 shows the average PAG sizes for future comparison with the substructures size. The grain axis distribution of all sections presents a broad range of minor and major axis dimensions varying from 2 to 29 μm and 4 to 69 μm, respectively. However, a high asymmetry is noticeable where the most frequent data are concentrated on the low-dimension side. In general, for all analysed areas, most of the PAG width and length are lower than 10 μm and 23 μm, respectively.

The top section has a significantly smaller grain size than the middle section outside the segregation bands. Within the middle section, it is possible to identify a difference between average grain sizes of the areas outside the segregation bands and within the segregation bands (SB), characterising a bimodal distribution of grains in this section. The effect of the presence of segregation bands can be seen by the average values of the whole field (middle including SB), which is slightly smaller than the middle outside SB.

Lath martensitic and bainitic grains can be described as PAGs divided into distinguishable packets subdivided into blocks consisting of laths. From {100} and {101} pole figures for all analysed areas

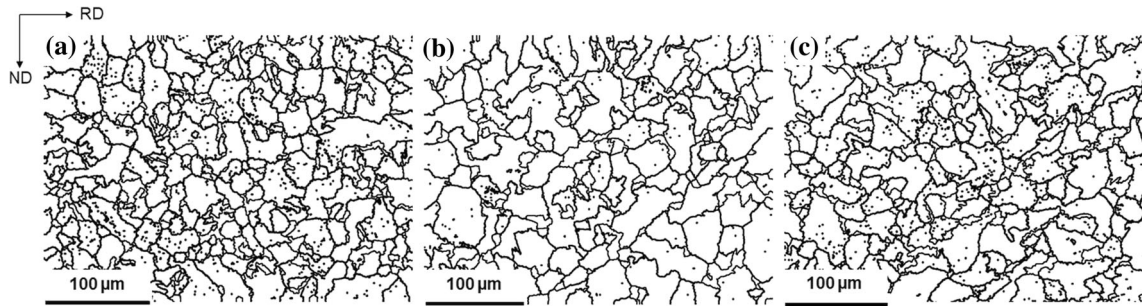


**Figure 11** Reconstructed prior austenite grains for a top, b middle outside segregation bands, and c middle including segregation bands.

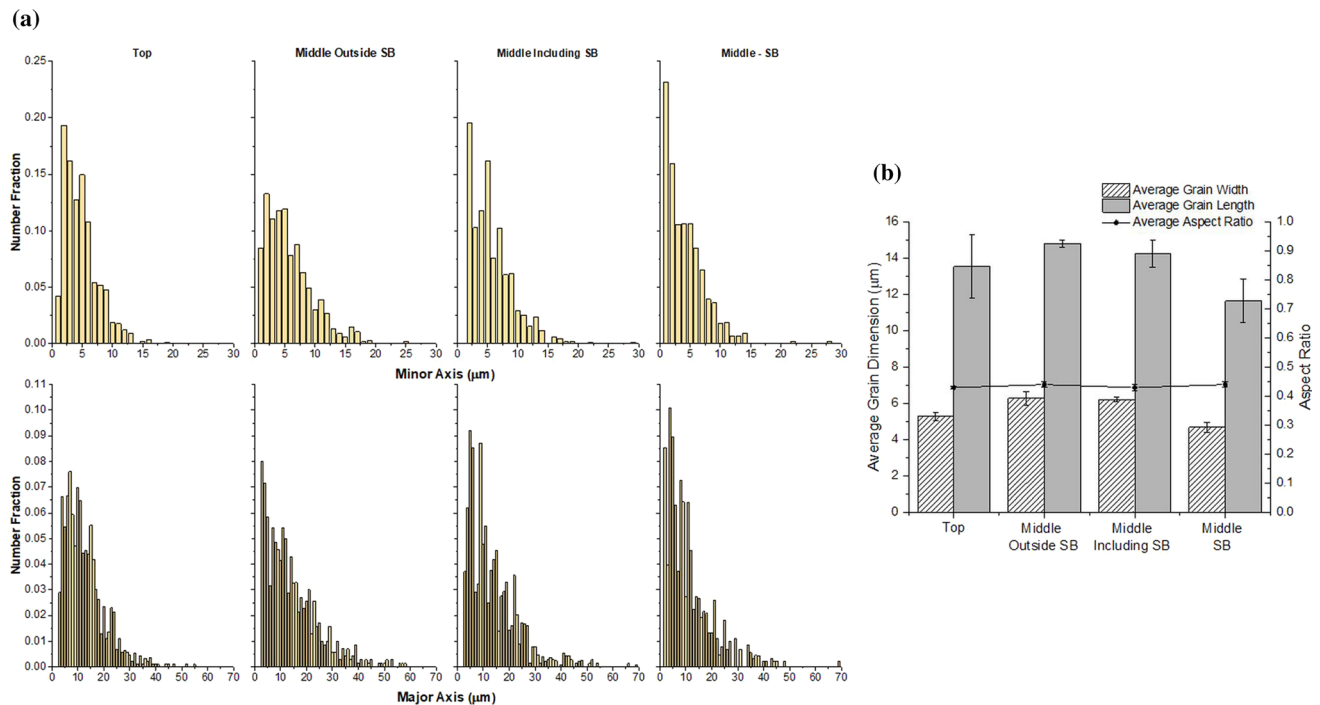


**Figure 12** Prior austenite grain size investigation represented as a distributions of their width and length, and b average values and aspect ratio for top, middle outside segregation bands, middle including segregation bands, and middle only in the segregation bands.

investigated in this work (Fig. 13), it is found that the crystallographic orientation relationship (OR) between the parent austenite phase and martensite or bainite for the S690QL steel being studied is the Kurdjumov–Sachs (K–S). The K–S OR has 24 variants, which are the different orientations that bcc phases can be formed within a single austenitic grain. These variants can be divided into four groups where each of these groups share the same  $\{111\}_{\text{austenite}} // \{110\}_{\text{martensite/bainite}}$  parallel relation of close-packed planes (same habit plane) [39].

As packets consist of sets of laths that share the same habit plane, packets can be distinguished by

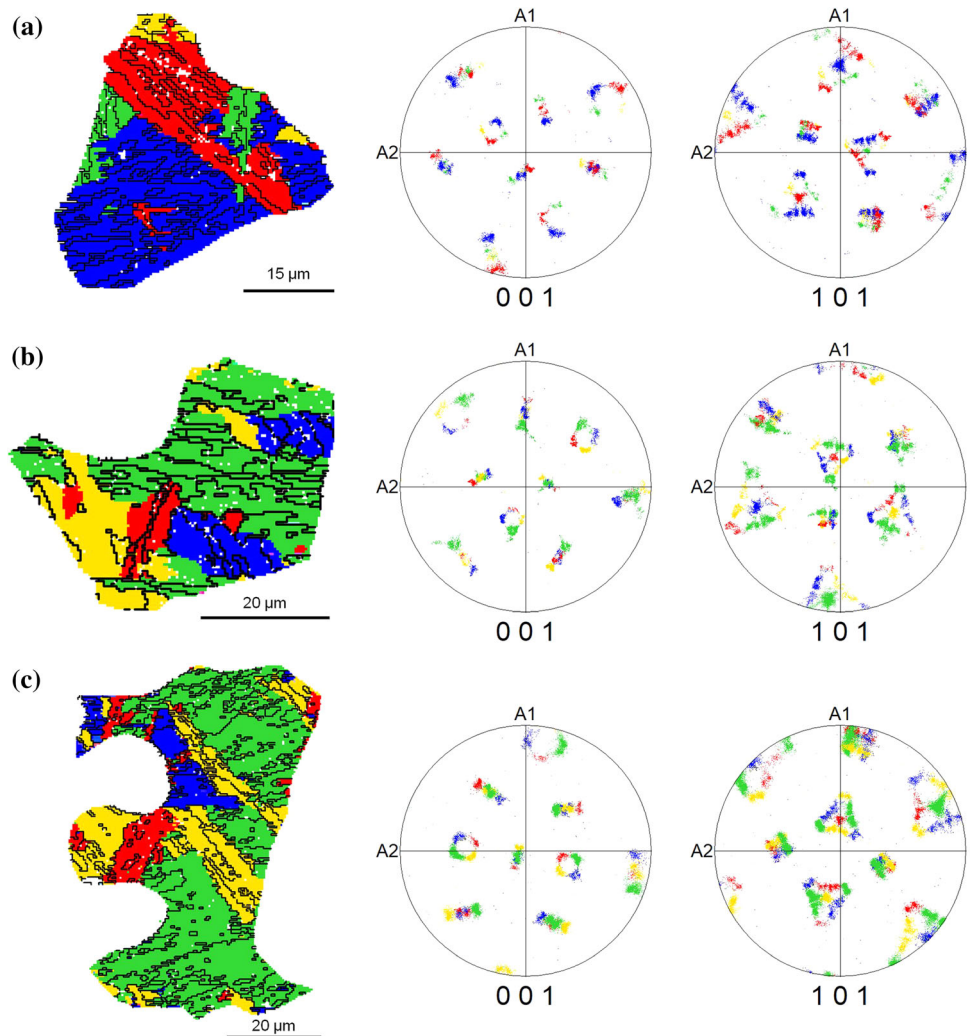
identifying the K–S OR variants from each group. This procedure was followed for each PAG, and Fig. 13 shows one prior austenite grain as an example. Blocks within a packet present the same habit plane and thus have the same colour in Fig. 13. Different packets and different variant groups are coloured in red, blue, green, and yellow. Black lines represent grain boundaries with misorientation angles higher than  $10^\circ$ , defining blocks.

Between 5 and 15 individual PAGs were cut from the EBSD maps of each analysed areas (top, middle outside CL, and middle including CL) to distinguish the different packets and the different blocks

**Table 4** Average width, length, and intercept size of prior austenite grains and their substructures for the top, middle outside segregation bands, middle including segregation bands, and middle only in the segregation bands sections of the S690QL steel plate

Area	Average PAG width ( $\mu\text{m}$ )	Average PAG length ( $\mu\text{m}$ )	Average intercept grain size ( $\mu\text{m}$ )	Average packet size ( $\mu\text{m}$ )	Average block width ( $\mu\text{m}$ )
Top	$5.3 \pm 0.2$	$13.5 \pm 1.8$	$19.2 \pm 1.4$	$10.1 \pm 2.8$	$2.0 \pm 0.3$
Middle outside SB	$6.3 \pm 0.4$	$14.8 \pm 0.2$	$23.5 \pm 2.3$	$12.2 \pm 3.5$	$3.0 \pm 0.6$
Middle including SB	$6.2 \pm 0.1$	$14.2 \pm 0.7$	$20.1 \pm 2.8$	$10.6 \pm 2.6$	$2.7 \pm 0.9$
Middle only within SB	$4.7 \pm 0.3$	$11.6 \pm 1.2$	$19.1 \pm 2.6$	$11.6 \pm 2.6$	$2.4 \pm 0.8$

**Figure 13** Prior austenite grains and (001) and (101) pole figures for **a** top, **b** middle outside segregation bands and **c** middle including segregation bands in which different packets and variant groups, that share the same habit plane, are coloured in the same colour (red, blue, green, or yellow). Black lines represent grain boundaries with misorientation angles higher than  $10^\circ$ , defining blocks.



allowing to measure their respective sizes. The average packet sizes and block widths are presented in Table 4. Slight variations are observed in the size of the packets when comparing the various investigated areas. However, all mean values are within the scatter. The same behaviour is observed for the measurement of the width of the blocks. No significant discrepancies were observed between regions.

EBSD may also help differentiate and quantify the bcc micro-constituents through their unique microstructural characteristics (e.g. lattice distortion and dislocation density) originating from their respective phase transformation processes that may affect diffraction parameters such as the grain average image quality.

The grain average image quality (GAIQ) distributions were plotted in the TSL-OIM software, and no

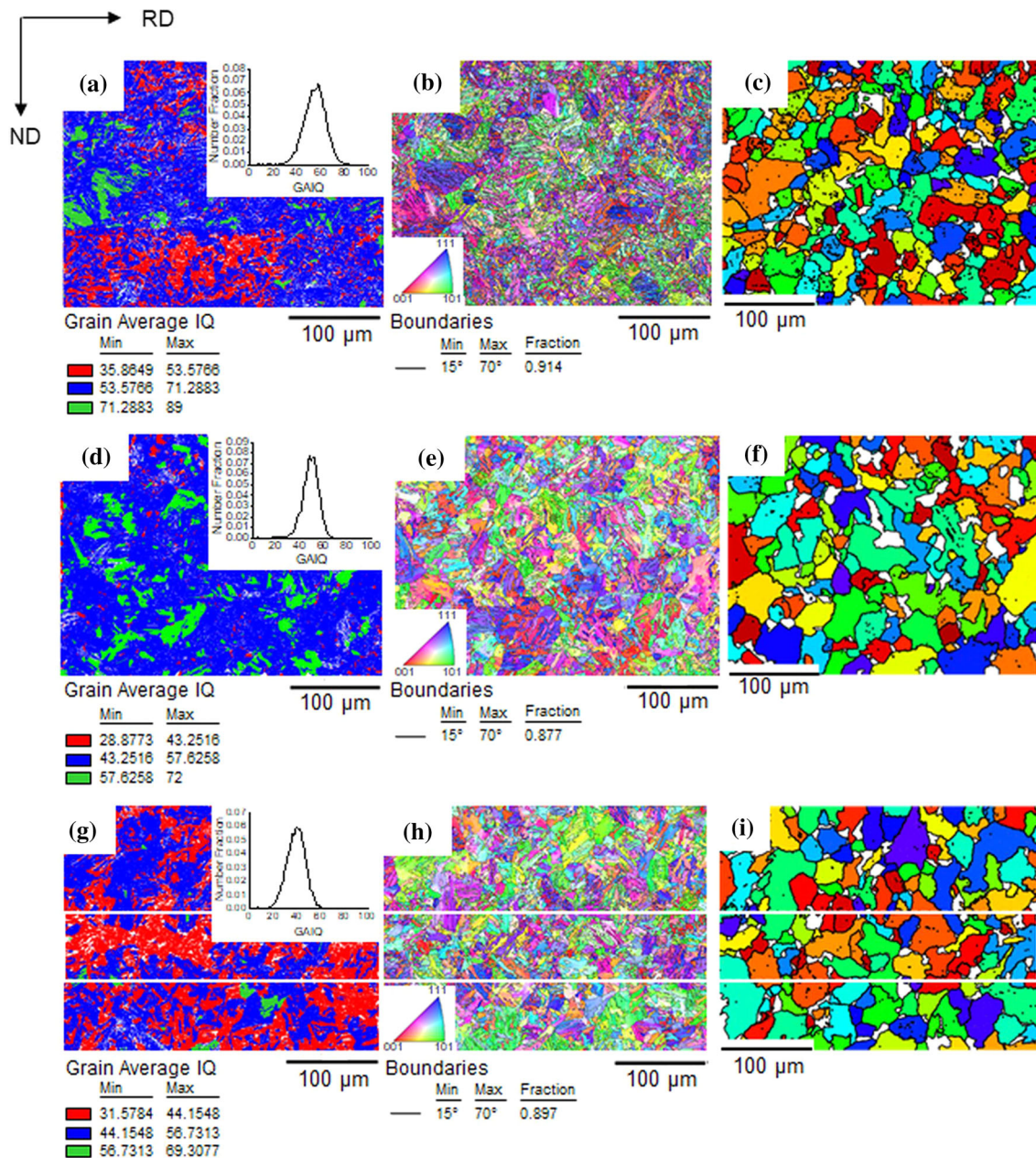


**Figure 14** Respective coloured GAIQ maps, ND inverse pole figures, and unique grain colour PAG maps reconstructed by the ARPGE software for the **a–c** top; **d–f** middle outside the segregation band; and **g–i** middle including the segregation band

clear distinction between multiple peaks could be made (Fig. 14a, d, g). A method to fit three peaks was applied in these distributions to dissociate the GAIQ peak into the contributions of different phases. However, for the minority of cases in which it was possible to dissociate GAIQ data into a maximum of three peaks, regarding the possibly present phases, the peaks strongly overlap. Hence, this method does

which is shown by the white rectangle. Martensite is indicated in red, bainite in blue, and ferrite in green in GAIQ maps (a), (d) and (g). The white grains in (c), (f), and (i) correspond to non-reconstructed areas.

not help define the threshold GAIQ values to distinguish the phases.

The TSL-OIM software indicates threshold values when generating colour-coded GAIQ maps based on the user's number of colours. In order to confirm and, when necessary, improve the definition of these values, a comparison of the colour-coded GAIQ map and the greyscale IQ map was performed.

EBSD areas for top and middle samples, outside the segregation bands and including areas outside and inside the segregation bands (further referred to as “middle outside SB” and “middle including SB,” respectively), were analysed. Figure 14 shows GAIQ maps, inverse pole figures, and reconstructed PAG maps for top and middle sections. In the GAIQ maps, green was chosen to represent ferrite (highest GAIQ values), blue to bainite, and red to martensite (lowest GAIQ values). Phase fractions based on the GAIQ method for each analysed area are shown in Table 5.

Based on GAIQ, martensite content is found larger in the top, which is compensated by the lower contents of ferrite and bainite. Moving towards the centre of the plate, a higher content of ferrite and bainite in the middle area outside segregation bands is observed. On the other hand, centreline segregation bands are observed to play a strong role in the middle section and stand out for presenting very much higher martensitic content—clearly banded structure in Fig. 14c, which, in turn, increase the martensitic content and, consequently, decrease the ferrite content. Although the results obtained through the GAIQ parameter fit with what is expected from the theoretical background and the results previously discussed, it is necessary to analyse the GAIQ maps more carefully, especially for tempered steel. For this, we will consider grain boundaries. According to the misorientation distribution of all grain boundaries, about 30–50% are martensitic lath boundaries (57°–65°) while approximately 10–20% are bainitic boundaries (48°–55°) in all analysed samples [40].

To confirm an area as a ferrite, a comparison between the three maps (GAIQ, inverse pole figures, and reconstructed prior austenite grains) was made, and three criteria were used: (1) the grain should present a high GAIQ; (2) the grain morphology shown in the inverse pole figure must not be lath-like; (3) the grain orientation should be homogeneous inside the grain. The possible ferrite grains that meet

these criteria were identified and then quantified. The results indicate that ferrite corresponds to 0.2% in the top section while the middle section outside the segregation bands and including the segregation bands contain approximately 0.4% and 0.1%, respectively.

Grain boundary misorientation angles can also bring relevant and helpful information regarding crack resistance through-thickness [4]. Figure 15 shows that the investigated areas display a very similar misorientation distribution, only differing in the intensity of some peaks.

The smallest fraction of misorientation angles in the range between 28° and 33° are attributed to high mobility boundaries mainly represented by the prior austenite grain boundaries [41]. In this range, no significant difference in the number fraction was observed between the sections. On the other hand, a larger fraction of misorientation angles above 48° is present in the top section.

### Hardness measurements

For a bulk analysis, the micro-Vickers hardness (HV<sub>3</sub>) was performed and the result as a function of distance from the top of the 80 mm S690QL steel plate is presented in Fig. 16. The S690QL steel plate displays a clear hardness gradient across the thickness where the outer surfaces of the plate are harder than the centre. The hardness profile also shows that there is a peak of hardness exactly in the middle of the plate (at a distance of 40 mm from the top). It is observed that the scatter increases in the areas closer to the mid-thickness.

A nanoindentation map was determined in the middle section, which is the most complex region of the steel, over a large area (320 × 320 μm<sup>2</sup>) to cover the maximum different microstructural zones observed in the material. This map is presented in Fig. 17. Figure 18 relates the nanohardness ranges for

**Table 5** Constituent’s fractions for top, middle outside segregation band (SB), middle including areas outside and inside SB and exclusively in the SB based on the GAIQ method

Microstructural constituent	Phase fraction (%)			
	Top	Middle outside SB	Middle including SB	Middle SB
Tempered martensite	22 ± 4	7 ± 6	29 ± 2	14.0 ± 0.5
Tempered bainite	68 ± 3	76 ± 3	64 ± 2	86 ± 3
Ferrite	6 ± 1	15 ± 3	3 ± 2	0.2 ± 0.1

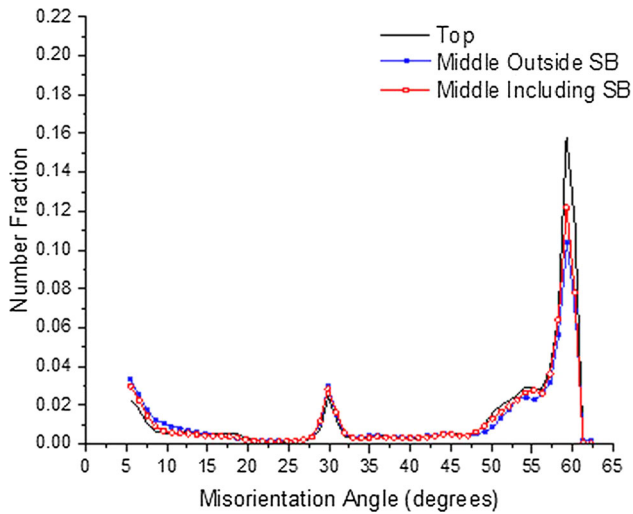


**Figure 15** Number fraction of boundary misorientation angles for the top, middle outside segregation bands, and middle including segregation bands sections.

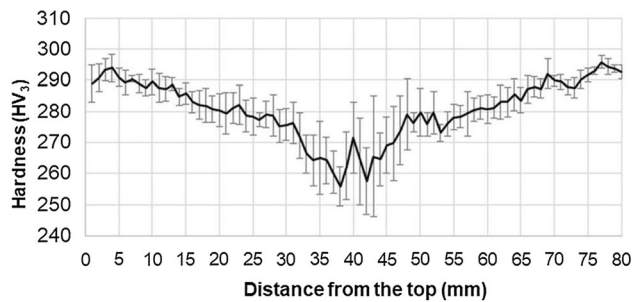


**Figure 16** Through-thickness micro-Vickers hardness ( $HV_3$ ) profile of the 80 mm S690QL steel plate. The error bars represent the standard deviation from the mean.

different areas within the map and presents their respective area fractions. The area fraction of zones with nanohardness of 7.33–8.62 GPa (red) and 8.62–9.75 GPa (dark red) area are so low that they do not appear in Fig. 18.

The contrasting microstructural areas located in the middle section have nanohardness values varying from 2.0 to 9.75 GPa. Blue, green, yellow, orange, red, and dark red zones correspond to the following hardness ranges: 2.00–2.80, 2.80–4.74, 4.74–5.55, 5.55–7.33, 7.33–8.62, and 8.62–9.75 GPa. The different zones will be further referred to by their colours. At first, what calls the most attention is how most of the harder zones (above 4.74 GPa) are densely concentrated and mainly distributed as horizontal lines parallel to the rolling direction at  $y = 130, 200,$  and  $270 \mu\text{m}$ . These lines refer to the centreline segregation bands. Inside the segregation bands, orange, red and

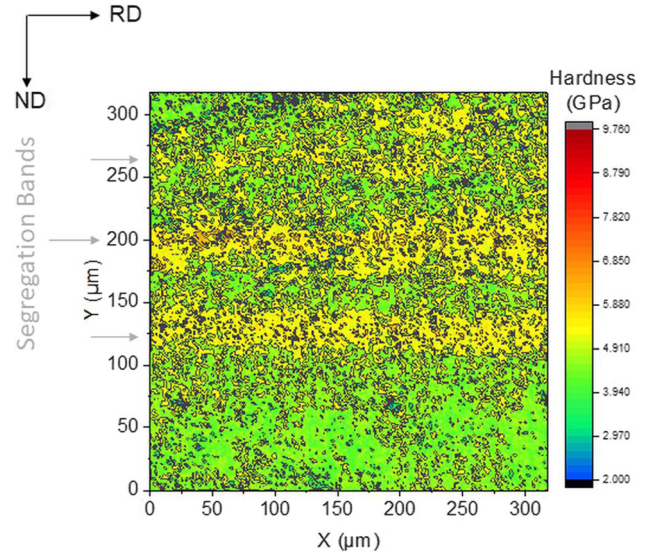


**Figure 17** Nanohardness map over a  $320 \times 320 \mu\text{m}^2$  area in the mid-thickness of the S690QL steel plate.

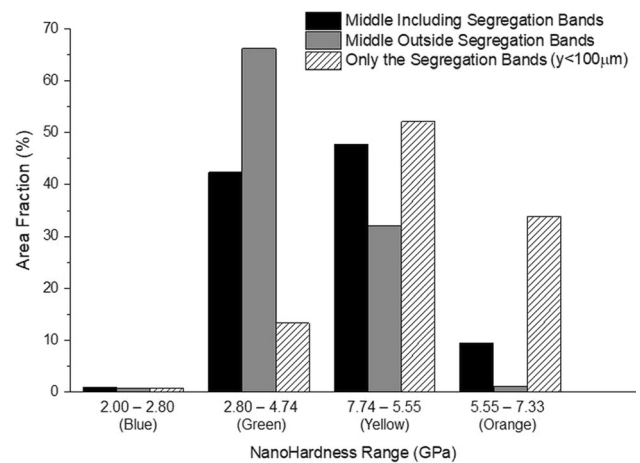


**Figure 18** Nanohardness ranges and their respective area fractions for each investigated zone in the map of Fig. 17. The area fraction of zones with nanohardness of 7.33–8.62 GPa (red) and 8.62–9.75 GPa (dark red) area significantly lower than the others (maximum of 0.1%) and, therefore, are not able to be presented at this scale.

dark red zones with higher hardness are present while outside the segregation bands, a mixture of yellow, green, and blue areas is observed. Regarding the blue areas, less than 1% of the map has the lowest nanohardness, between 2 and 2.8 GPa.

The areas of transition between blue and green colours and green and yellow colours have the largest mechanical heterogeneity. Nevertheless, the blue/green interfaces are small since the area fraction of the first represents 1% of the entire map while the



**Table 6** CTOD results for top and middle thickness positions in T-L orientation tested at  $-100\text{ }^{\circ}\text{C}$ 

Thickness position	Minimum CTOD (mm)	Maximum CTOD (mm)	Average CTOD (mm)
Top	0.022	0.074	$0.048 \pm 0.019$
Middle	0.010	0.020	$0.012 \pm 0.004$

green/yellow is extensive due to the segregation bands planes.

In an attempt to correlate the different hardness areas with the different microstructural zones, helping to distinguish the different BCC constituents, EBSD and SEM analysis were performed on the indentation map. Regarding EBSD, no correlation was found. Therefore, despite providing a rough estimate and indicating potential critical fracture zones, EBSD and nanoindentation cannot be used to accurately distinguish between BCC structural constituents for the quenched and tempered S690 high strength steel studied herein. In the case of SEM analysis, two main problems were observed that prevented the analysis of the etched nanoindentation map to be carried out. The first one is that, during EBSD analysis, the areas where the electron beam makes contact with the surface to acquire the diffraction patterns, a contamination layer is built. Due to the presence of this layer, the etchant has no effect and the material remains unetched in the previously analysed EBSD areas. The second problem is that, due to the small depth of the indents (around  $70\text{ }\mu\text{m}$ ), the etching procedure completely removed the residual imprint of the indentation, not being able to locate the indents afterwards.

### Through-thickness fracture behaviour

Three-point bending tests were performed at  $-100\text{ }^{\circ}\text{C}$  in the top and middle sections of the S690QT steel plate. The minimum, maximum and average CTOD results including their standard deviation from the average values are shown in Table 6. As can be seen, the middle section presents a lower fracture toughness and a lower scatter than the top section.

## Discussion

### Through-thickness microstructural inhomogeneity

In this study, the comprehensive microstructural characterisation of the S690 HSS demonstrated that

the microstructure significantly varies through the thickness. Through the processing route, the steel plate experiences uneven strain levels and cooling rates. Consequently, the top and middle sections present distinctly different microstructural composition.

In terms of bcc micro-constituents distinction and quantification, different techniques were used: dilatometry, microscopy and nanoindentation. The dilatometric analysis suggests the presence of martensite and bainite after quenching, while the microscopic investigation indicates the presence of grains that resemble tempered bainite, tempered martensite and ferrite, as also predicted by the CCT diagrams. Ferrite grains were quantified from the SEM micrographs and the results show that each position in the thickness contains around 0.2% of ferrite. Consequently, this phase is present in a too small fraction to be detected by the dilatometric curve. EBSD was also used through the analysis of GAIQ maps in an attempt to assist the distinction of bcc micro-constituents. However, in the case of tempered steels such as the currently investigated steel, the use of GAIQ for phase distinction may be less effective, since during the heat treatment, the saturated carbon in solid solution, specifically for martensitic grains, diffuses out and possibly forms carbides, the dislocation density is reduced, and the residual stress in the crystal is relieved. Consequently, the phase's diffraction pattern is sharpened, leading to an approximation, and possible overlap, of the GAIQ values. As a result, it is difficult to define the threshold GAIQ values. Hence, an estimation may be made, but an accurate analysis is not possible. According to the analysis via GAIQ maps, the martensitic fraction is larger in the top section while the ferritic and bainitic fractions are larger in the middle outside of the segregation band. This result is in line with the expectation where a faster cooling during the quenching process occurs in the outer surface of the steel plate, as can be seen in Fig. 2a. Moreover, the middle section was observed to have a clear banded structure—centreline segregation bands—with grains of very low GAIQ. As presented

in the EPMA results and Ms and Bs transformation temperatures in Fig. 9, the segregated alloying elements (e.g. Mo, Cr, and Mn) facilitate the formation of martensite, resulting in a greater fraction. During cooling, the bainitic transformation occurs initially in areas with lower solute content due to higher  $B_s$  temperature, rejecting carbon to areas recognised as high-solution regions, enriching them even more. It is known that the alloying elements that identify segregation in the bands slow down the transformation kinetics (e.g. austenite to ferrite), shifting the CCT curve (Fig. 6) to longer times and, thus, increasing steel's hardenability [42, 43]. Hence, at the same cooling rate at the central part of the plate (5 °C/s) as the regions with lower content of alloying elements, where the microstructure is composed of a mixture of ferrite, bainite, and martensite, greater martensite and lower or zero ferrite fractions are expected in the segregation bands. Nevertheless, it is worth mentioning that the elemental segregation by itself may cause distortion in the lattice and contribute to the low GAIQ in the segregation bands. The discussion on the use of nanoindentation to distinguish bcc micro-constituents by their local properties will be presented in “[Microstructure—hardness relationship](#)” section.

The misorientation distribution of martensitic and bainitic grain boundaries were also analysed. Contrary to the phase fraction measured by the GAIQ values, the misorientation values at grain boundaries indicate that martensite is present in a larger fraction than bainite. Moreover, it also suggests that areas identified as bainite by the GAIQ map not only refer to bainite but also to martensite, which, when tempered, has its diffraction pattern improved, approaching image quality values close to that of bainite, which, as a result, leads to a misidentification as bainite.

For the ferritic quantification based on the GAIQ values, it was observed that grains mistakenly indexed as ferrite in Fig. 14 may be tempered bainite or low-carbon tempered martensite. The regions corresponding only to the segregation bands do not contain ferrite grains. These fractions are per the quantification made based on the micrographs obtained by SEM and also in accordance with the theoretical background discussed above.

Therefore, although the GAIQ method gives a rough estimation of phase fractions and distribution of these bcc phases in different sections, it is still

necessary to propose other methods to differentiate and accurately quantify them. For this purpose, we propose a correlative approach by using a combination of techniques which include nanoindentation measurements.

Most inclusions through the thickness of the plate have a complex chemical composition. This complexity is due to the fact that pre-existing inclusions serve as a site for nucleation and subsequent growth of other inclusions such as titanium nitrides (TiN) on the surface of oxide inclusions, niobium carbides (NbC) on the surface of TiN, and manganese sulphide (MnS) on oxides ( $Al_2O_3$ -MgO) as observed by [1, 44, 45]. Oxide inclusions were found to be of the same size and area fraction in the top and middle sections while Nb-rich inclusions were found in a greater area fraction and larger sizes in the middle section. This can be attributed to their different nucleation/growth steps in the steelmaking process. The nucleation of oxides and sulphides occur during the secondary metallurgy (e.g. in the alloying addition) and are homogeneously distributed afterwards in the liquid steel. During solidification, these inclusions are captured by growing dendrites and are homogeneously distributed through the thickness along the solidification process. For the Nb-rich inclusions that nucleate and grow in the liquid state during casting, the cooling gradient through the thickness and the elemental segregation in the middle section have a major effect. In thick slabs, the temperature in the central part of the slab takes longer to dissipate and the centre of the slab remains as a liquid while the solidification process in the outer surface of the slab had already started. Consequently, the inclusion nucleation and growth processes continue, resulting in larger content and sizes of inclusions in the middle section. The elemental segregation in the middle of the slab also leads to larger chance of reaching the solubility limits of the elements in the liquid, increasing the probability to form these inclusions in the middle section. Moreover, defects were observed in middle-section inclusions as shown in Fig. 7d–f. These defects may have originated during the rolling process due to a combination of factors such as the rolling stress and the brittle nature of such inclusions. Nevertheless, the sample preparation procedure, already known for breaking or tearing inclusions out of the matrix, should also be considered as influencing the formation of defects. Da Costa e Silva [46] reports the effect

of hot rolling deformation on different inclusions. Usually, brittle inclusions are more likely to crack or break under rolling stress. Moreover, the interfacial strength between the inclusion and the matrix is low, which causes the interface to act as a source of microvoid and crack formation [47]. In the case of coarse and irregular-shaped inclusions, such as those found in the presently studied S690QL steel, the consequences can be more severe since a high stress concentration is generated in the sharp interfacial corners, and cracks can nucleate and grow at the interfaces of the inclusions under the rolling load, even in steels of which the matrix has a relatively high ductility [47].

Several authors report the effects of PAG size of lath martensitic and lath bainitic grains and their microstructural units that present high-angle boundaries (e.g. packets and blocks) on strength, toughness, and crack propagation [39, 48–52]. Therefore, the grain sizes in the top and middle sections were measured and compared. In the top section of the steel plate, the PAG are slightly smaller than the ones in the middle section outside the segregation bands (Fig. 12b). This agrees with expectations that high strain values are reached in the surface and decrease through the thickness during rolling [53] and as a result, more defect energy, determining recrystallization, is stored by the material close to the surface than in the centre of the plate. Hence, the austenite recrystallization during hot rolling tends to lead to a more refined grain structure in the outer part of the slab. Within the middle section, the average PAG sizes in the areas outside the segregation bands and within the segregation bands (SB) are different (Fig. 12b) and, characterise a bimodal distribution of grain sizes. The smaller grain sizes found in the segregation bands may be explained by the solute drag effect where segregated elements retard the grain boundary migration and slow down the grain growth, and also the Nb-rich cubic inclusions observed along the PAG boundaries (Fig. 7e) pinning grain boundaries [54]. Moreover, Reiter, Bernhard, and Presslinger [55] reported, through a study of the austenite grain size during casting, that the equivalent carbon content ( $c_p = x_c - 0.14 x_{Si} + 0.04 x_{Mn}$ , where  $x_i$  is the weight percentage of element  $i$ ) can influence the grain size [55]. According to the authors, when  $c_p$  is larger than 0.17%, the grain size decreases with increasing  $c_p$  value [55]. The parameter  $c_p$  was calculated based on the EPMA line scans

through the segregation bands. The results show that a significant fraction of the segregation band width has  $c_p > 0.17\%$ . Furthermore,  $c_p$  may reach values up to 0.37%, where the bands with smaller widths have a higher number of areas with  $c_p$  values  $> 0.17\%$ . Therefore, narrower segregation bands might present smaller PAG and larger relative frequency of small grains. Regarding the PAG substructures (e.g. packets and blocks), as the prior austenite grain sizes (Table 4) of the analysed regions do not present major differences, large variations in the size of PAG substructures are not detected. No significant discrepancies were observed between the investigated regions.

### Microstructure—hardness relationship

The hardness gradient through the 80 mm thickness of the S690QL HSS plate reflects the different microstructural composition of the top and middle sections in terms of the fraction of micro-constituents and prior austenite grain sizes. The lower fraction of hard martensite and larger PAG sizes in the centre lead to a lower hardness compared to the top section. The peak of hardness in the central part of the plate can be attributed to the presence of centreline segregation bands which are likely to have higher hardness due to the solute segregation that serve as barriers to dislocations during plastic deformation, larger content of martensite, the cluster of brittle Nb-rich inclusions and smaller prior austenite grain size than the surrounding areas. Through the middle section, a large scatter in the hardness measurements in the middle section is due to the mixture of transformation products with different hardness, banded microstructure with interspersed enriched and depleted zones with different hardness, PAG sizes, and brittle inclusions distribution.

From the micro-Vickers hardness measurements, it was shown that the micro-scale hardness measurements cannot be used to accurately evaluate the microstructural variations and single microstructural features that exist in fine-structured multiphase steels like the S690QL steel under study. Therefore, nanoindentation analyses are essential to bring a more in-depth knowledge regarding local microstructural and property inhomogeneities, individual behaviours, and their combined effect on mechanical properties and fracture behaviour. The segregation bands were observed to be the harder

area in the steel plate. Their hardness reach values up to 2.4 times that of surrounding areas, which is likely to affect the material's crack resistance and mechanical and fracture performance. As already discussed, the largest hardness in segregation bands is due to the combined effect of solute segregation, the predominantly martensitic structure, smaller PAG size than the surrounding areas, and the presence of Nb-rich brittle inclusions. Inside of the segregation bands, some areas present higher hardness than the average value for the band. Areas with hardness varying from 5.55 to 7.33 GPa (orange areas in the hardness map of Fig. 17) are present in a large area fraction (34%), and thus, it is unrealistic to consider them clusters of brittle inclusions, but they may be representing high-carbon martensite grains. Areas with the highest hardness level, 7.33–9.75 GPa (red and dark red zones in Fig. 17) exist in an area fraction similar to that estimated for brittle inclusions within these areas by optical microscopy, suggesting that these second-phase particles can be responsible for the largest hardness. Outside the segregation bands, the material presents hardness varying from 2.8 to 5.55 GPa (yellow and green areas in Fig. 17) which is likely to be representing tempered bainite and tempered low-carbon martensite. Within this area, the hardness is constantly alternating at a distance less than a typical PAG size, showing a certain degree of heterogeneity inside lath grains attributed to their substructures [18]. Only a few areas (1%) present a hardness range of 2.00–2.80 GPa (blue areas in Fig. 17). These values agree with the ones reported in the literature for ferrite after tempering [19, 56]. Although a comparison with other studies can be made, the testing parameters used herein may differ from other research, and the direct comparison is uncertain. The area fraction of ferrite estimated from the nanoindentation results are within the estimated value from SEM and EBSD analysis.

Therefore, from the nanoindentation measurements, the local properties variation provides indications about the different phases, but it was not possible to distinguish them precisely. Due to the tempering process, the nanohardness values for different phases come closer together with an overlap. Consequently, the accurate distinction of the phases through their properties is not possible.

### Potential microstructural aspects affecting fracture toughness

The through-thickness microstructural analyses and the hardness measurements pointed out the differences between the top and middle sections that can significantly influence the fracture behaviour of the steel under study. Hence, these results provide evidence of the through-thickness potential critical sites for fracture and the most detrimental thickness section in the steel plate.

The top and middle sections differ microstructurally mainly by characteristics of inclusions, the size of the PAG and their distribution of misorientation at grain boundaries. The middle section presents a larger volume fraction of inclusions, mainly the cubic-shaped ones, which are known for acting as cleavage crack nucleation sites [57]. Hence, more potential initiation sites are present in the middle section. These inclusions are also present in larger sizes, which means that once the fracture process is initiated inside them, the initial crack will have a larger size in the middle than the top section. As a consequence, the fracture stress is lower in the middle [58]. This initial crack length can be even larger when cubic inclusions are dispersed close to each other in clusters, being considered as one single large inclusion, as discussed in “[Through-thickness microstructural characterisation](#)” section, further reducing the required stress to fracture. Furthermore, inclusions, mostly cubic, in the middle section were also usually associated with defects in themselves and at the interface inclusion/matrix. In this case, these inclusions potentially characterise an easy path for crack propagation. Regarding the grain size and the distribution of misorientation at grain boundaries, both parameters can affect the propagation of fracture micromechanism affecting fracture toughness [59]. The middle section presents the larger grain sizes and smaller fraction of high-angle grain boundaries than the top, which reduces the stress needed for fracture and the crack resistance, respectively.

In terms of hardness variation, the nanoindentation map highlights the microstructural variation and its effects on nanohardness in the middle section. Due to the significant hardness difference between the segregation bands and the matrix, their interface would be preferential sites for crack formation due to the

high probability of interfacial separation and can be responsible for fracture toughness reduction [22, 23].

The three-point bending tests at  $-100\text{ }^{\circ}\text{C}$  show that, in line with the microstructural and hardness analyses performed by the comprehensive quantitative characterisation, the middle section has lower cleavage fracture toughness and, therefore, is more detrimental than the top. Another important aspect is that the lower standard deviation for the middle may indicate that, even though the through-thickness microstructure of the material is inhomogeneous, the microstructure of the middle section as a whole is more brittle and critical than the top. A continuation of this work will focus on investigating the fracture surfaces of tested CTOD specimens to identify the weak microstructural features and to study the initiation and propagation micromechanisms of cleavage failure in the 80 mm thick quenched and tempered S690 high strength steel.

## Conclusions

In order to identify the potential weak microstructural sites on fracture at low-temperature applications, a correlative approach was proposed to characterise and quantify the through-thickness complex and heterogeneous microstructure of the 80 mm thick quenched and tempered S690 high strength steel plate. The study resulted in the following conclusions:

1. The combined analysis via dilatometry, CCT diagrams and SEM showed that a mixed tempered microstructure including ferrite, bainite and martensite is present through the entire thickness, where ferrite represents less than 1% of the phases. However, microstructural variations were observed in terms of grain size, inclusion content, and elemental segregation.
2. The PAG size slightly increases as it approaches the centre of the plate, except for the centreline segregation bands found in the middle section. The middle section exhibits a bimodal grain size distribution where grains outside the segregation bands are slightly larger than the top section, but PAG inside segregation bands are smaller than the top. Nevertheless, there was no significant difference in packet size and block width over thickness. This is due to the slight variation in the grain size of the prior austenite between the sections.
3. In terms of inclusions, the most commonly observed particles have spherical and cubic morphologies and complex chemical compositions of oxides, carbides, and nitrides throughout the thickness. Although the analysed thickness positions have circular inclusions of the same size range, the middle of the plate presents larger cubic inclusions that are often distributed as clusters, a greater amount of spherical and cubic particles than the top. Note that these clusters of cubic inclusions may be considered a line of collinear inclusions reaching sizes larger than four times the size of cubic inclusions in the top. Additionally, defects in the interface inclusion/matrix and the inclusion itself were observed in the middle.
4. The chemical composition analysis through the centreline segregation bands indicates that Mo, Mn, Cr, Si, Ni, and C are the elements that segregate in these areas. By calculating the phase transformation temperatures for bainite and martensite based on the chemical composition variation through the bands, it is clear that elemental segregation affects the microstructural transformation and, consequently, the phase fractions found in these areas. Hence, greater martensite and lower or no ferrite fractions are expected in the segregation bands.
5. For the S690QL high strength steel studied herein, the EBSD analysis does not accurately distinguish bcc phases based on the GAIQ and boundary misorientation angles. The misorientation distribution of martensitic and bainitic boundaries shows that some areas, identified as bainite from the GAIQ method, refer to martensite, which had their image quality improved during the tempering process. Additionally, some lath grains were mistakenly indexed as ferrite due to their high image quality values. Nevertheless, it gives a rough estimation of the micro-constituents and their fraction in the material. The GAIQ procedure indicates higher martensitic and lower ferritic content in the top section, which is a consequence of the faster cooling process in the outer part of the plate compared to the mid-thickness during the quenching process. On the other hand, centreline segregation bands present a higher martensitic

content than the middle outside the segregation band due to the elemental segregation, which, in turn, scale up the martensitic content. Moreover, EBSD data allowed the investigation of misorientation boundary distribution in all sections, indicating that the top section has the largest fraction of high-angle grain boundaries ( $> 15^\circ$ ) and the middle section has the largest fraction of low-angle grain boundaries ( $< 15^\circ$ ).

6. Micro-Vickers measurements showed a clear bulk hardness gradient through the thickness, where the harder areas belong to the outer surfaces of the plate. This result is directly related to the microstructural observations regarding the area fraction of micro-constituents and PAG sizes. On the one hand, the top section has a larger area fraction of martensite and smaller PAG sizes, which increase their hardness. On the other hand, in the general middle section, the martensitic fraction is lower, and the grains sizes are larger, which reduces their hardness. However, a peak of hardness right in the central part of the plate is attributed to the presence of segregation bands with a larger area fraction of martensite than the middle outside the segregation bands, the smallest grain sizes of the entire thickness, the presence of clusters of hard inclusions, and solute segregation act as barriers for dislocation movements.
7. In the nanoscale, the dense and large nanoindentation map in the middle section—the most complex area of the material—shows that the centreline segregation bands are the hardest zones reaching values up to 2.4 times higher than the hardness of surrounding areas. The highest hardness gradient was observed in the interface between the matrix and the segregation bands. Consequently, this would be the preferential site for crack formation due to the high chance of interfacial separation and the reduction in fracture toughness. Regarding the phase distinction through properties, although the local properties variation indicates different phases, it was not possible to distinguish them accurately. Due to the tempering process, the nanohardness values overlap for the different phases, making their distinction difficult. Additionally, although the use of EBSD and nanoindentation provide a rough estimate of constituents' fraction and indication of potential critical fracture zones, they cannot be used to accurately distinguish between

BCC structural constituents for the S690QL high strength steel under study.

8. The top section of the HSSs plate displays a higher fracture toughness than the middle section. Moreover, a high scatter in the CTOD values is observed for the top section, while in the middle it is very low. This behaviour can be explained by the more detrimental microstructure present in the middle section (e.g. clusters of Nb-rich inclusions, larger Nb-rich inclusions and long interfaces with large hardness gradients) than in the top, as suggested by the quantitative microstructural characterisation.

Therefore, the comprehensive microstructural characterisation and quantification of this high strength steel suggests that the plate's middle section is the most critical area in mechanical and fracture behaviours, being likely to affect the global material performance and the reliability of structural components. This unfavourability of the middle section is attributed to its larger prior austenite grain sizes, larger sizes and area fraction of inclusions, the presence of defects associated with the circular and cubic inclusions and with their interface with the matrix, clusters of cubic inclusions that may also be distributed along the PAG boundaries, and the long interfaces with the largest hardness gradients. All these factors make the middle section more prone to crack initiation and more likely to present the lowest fracture toughness of the S690QL high strength steel. Future work will focus on investigating the impact of the presented microstructural inhomogeneities on cleavage fracture toughness and damage micromechanisms of the commercially available 80 mm thick quenched and tempered S690 high strength steel allowing the confirmation of the weak microstructural features. This will be done through both modelling and experimental approaches.

### Data availability statement

The raw/processed data required to reproduce these findings cannot be shared at this time as the data also form part of an ongoing study.

## Acknowledgements

The authors acknowledge the support in the Micro-Tough research project (n. 16350) from the Dutch Research Council (NWO) and the consortium of partners that include Allseas Engineering, Dillinger, Lloyd's Register, The Dutch Ministry of Defence, and TNO. We also acknowledge Ruud Hendrikx and C. Kwakernaak from the Surfaces & Interfaces group of TU Delft for performing the XRF and EPMA analysis, respectively, and Nico Geerlofs from the Microstructure group of TU Delft and Eliseo Hernández Durán from the Department of Electromechanical, Systems and Metal Engineering of Ghent University for performing dilatometry experiments.

## Author contribution

VB contributed to conceptualization, methodology, validation, formal analysis, investigation, resources, data curation, writing—original draft, writing—review and editing. QJ contributed to conceptualization, methodology, formal analysis, resources, writing—review and editing. SS contributed to conceptualization, resources, writing—review and editing. RHP contributed to conceptualization, methodology, formal analysis, resources, writing—review and editing. UH contributed to conceptualization, methodology, formal analysis, resources, writing—review and editing. CW contributed to conceptualization, validation, writing—review and editing, supervision. JS contributed to conceptualization, validation, writing—review and editing, supervision. VP contributed to conceptualization, validation, writing—review and editing, supervision, project administration.

## Declarations

**Conflict of interest** The authors declare that they have no known competing financial interests or personal relationships that could have appeared to influence the work reported in this paper.

**Open Access** This article is licensed under a Creative Commons Attribution 4.0 International License, which permits use, sharing, adaptation, distribution and reproduction in any medium or format, as long as you give appropriate credit to the original author(s) and the source, provide a link to the

Creative Commons licence, and indicate if changes were made. The images or other third party material in this article are included in the article's Creative Commons licence, unless indicated otherwise in a credit line to the material. If material is not included in the article's Creative Commons licence and your intended use is not permitted by statutory regulation or exceeds the permitted use, you will need to obtain permission directly from the copyright holder. To view a copy of this licence, visit <http://creativecommons.org/licenses/by/4.0/>.

## References

- [1] Popovich V, Richardson IM (2015) Fracture toughness of welded thick section high strength steels. In: TMS 2015 144th annual meeting & exhibition: supplemental proceedings. Springer International Publishing: Cham, pp 1031–1038. <https://doi.org/10.1002/9781119093466.ch125>
- [2] Wang Q, Ye Q, Wang Z et al (2020) Thickness effect on microstructure, strength, and toughness of a quenched and tempered 178 mm thickness steel plate. *Metals (Basel)* 10:1–16. <https://doi.org/10.3390/met10050572>
- [3] Bertolo VM, Jiang Q, Walters CL, Popovich VA (2020) Effect of microstructure on cleavage fracture of thick-section quenched and tempered S690 high-strength steel. In: Characterization of minerals, metals and materials 2020. San Diego, pp 155–168
- [4] Liu H, Zhang H, Li J (2018) Thickness dependence of toughness in ultra-heavy low-alloyed steel plate after quenching and tempering. *Metals (Basel)*. 8:1–11. <https://doi.org/10.3390/met8080628>
- [5] Moore P, Yordanova B, Lu Y, Janin YJ (2019) Influence of microstructural variation in thick section steels on the characterisation of fracture toughness using sub-size specimens. In: Proceedings of the ASME 2019 38th international conference on ocean, offshore and arctic engineering OMAE 2019. <https://doi.org/10.1115/OMAE2019-96010>
- [6] Wallin K (2015) Master curve analysis of ductile to brittle transition region fracture toughness round robin data. The “EURO” fracture toughness curve. Tech. Res. Cent. Finland, VTT Publ. 367
- [7] Andrieu A, Pineau A, Besson J et al (2012) Beremin model: methodology and application to the prediction of the Euro toughness data set. *Eng Fract Mech* 95:102–117. <https://doi.org/10.1016/J.ENGFRACMECH.2011.10.019>
- [8] Pineau A (2006) Development of the local approach to fracture over the past 25 years: theory and applications. *Int J*

- Fract 138:139–166. <https://doi.org/10.1007/s10704-006-0035-1>
- [9] Jiang Q, Bertolo VM, Popovich VA, Walters CL (2019) Recent developments and challenges of cleavage fracture modelling in steels: aspects on microstructural mechanics and local approach methods. In: Proceedings of the ASME 2019 38th international conference on ocean, offshore and arctic engineering OMAE 2019. <https://doi.org/10.1115/OMAE2019-95464>
- [10] Lin T, Evans AG, Ritchie RO (1986) A statistical model of brittle fracture by transgranular cleavage. *J Mech Phys Solids* 34:477–497. [https://doi.org/10.1016/0022-5096\(86\)90013-X](https://doi.org/10.1016/0022-5096(86)90013-X)
- [11] Martín-Meizoso A, Ocaña-Arizcorreta I, Gil-Sevillano J, Fuentes-Pérez M (1994) Modelling cleavage fracture of bainitic steels. *Acta Metall Mater* 42:2057–2068. [https://doi.org/10.1016/0956-7151\(94\)90031-0](https://doi.org/10.1016/0956-7151(94)90031-0)
- [12] Kroon M, Faleskog J (2005) Micromechanics of cleavage fracture initiation in ferritic steels by carbide cracking. *J Mech Phys Solids* 53:171–196. <https://doi.org/10.1016/J.JMPS.2004.05.008>
- [13] Chen JH, Li G, Cao R, Fang XY (2010) Micromechanism of cleavage fracture at the lower shelf transition temperatures of a C–Mn steel. *Mater Sci Eng A* 527:5044–5054. <https://doi.org/10.1016/j.msea.2010.04.063>
- [14] Navarro-López A, Hidalgo J, Sietsma J, Santofimia MJ (2017) Characterization of bainitic/martensitic structures formed in isothermal treatments below the Ms temperature. *Mater Charact* 128:248–256. <https://doi.org/10.1016/j.matchar.2017.04.007>
- [15] Papaefthymiou S, Banis A, Bouzouni M, Petrov RH (2019) Effect of ultra-fast heat treatment on the subsequent formation of mixed martensitic/bainitic microstructure with carbides in a CrMo medium. *Metals (Basel)* 9:1–14. <https://doi.org/10.3390/met9030312>
- [16] Petrov R, Kestens L, Wasilkowska A, Houbaert Y (2007) Microstructure and texture of a lightly deformed TRIP-assisted steel characterized by means of the EBSD technique. *Mater Sci Eng A* 447:285–297. <https://doi.org/10.1016/j.msea.2006.10.023>
- [17] Zhu K, Barbier D, Iung T (2012) Characterization and quantification methods of complex BCC matrix microstructures in advanced high strength steels. *J Mater Sci.* 48:413–423. <https://doi.org/10.1007/s10853-012-6756-9>
- [18] Chang Y, Lin M, Hangen U et al (2021) Revealing the relation between microstructural heterogeneities and local mechanical properties of complex-phase steel by correlative electron microscopy and nanoindentation characterization. *Mater Des* 203:1–11. <https://doi.org/10.1016/j.matdes.2021.109620>
- [19] Baltazar Hernandez VH, Panda SK, Kuntz ML, Zhou Y (2010) Nanoindentation and microstructure analysis of resistance spot welded dual phase steel. *Mater Lett* 64:207–210. <https://doi.org/10.1016/j.matlet.2009.10.040>
- [20] Busby JT, Hash MC, Was GS (2005) The relationship between hardness and yield stress in irradiated austenitic and ferritic steels. *J Nucl Mater* 336:267–278. <https://doi.org/10.1016/j.jnucmat.2004.09.024>
- [21] Ariza-Echeverri EA, Masoumi M, Nishikawa AS et al (2020) Development of a new generation of quench and partitioning steels: Influence of processing parameters on texture, nanoindentation, and mechanical properties. *Mater Des* 186:1–17. <https://doi.org/10.1016/j.matdes.2019.108329>
- [22] Hidalgo J, Celada-Casero C, Santofimia MJ (2019) Fracture mechanisms and microstructure in a medium Mn quenching and partitioning steel exhibiting macrosegregation. *Mater Sci Eng A* 754:766–777. <https://doi.org/10.1016/j.msea.2019.03.055>
- [23] Lee SG, Kim B, Sohn SS et al (2019) Effects of local-brittle-zone (LBZ) microstructures on crack initiation and propagation in three Mo-added high-strength low-alloy (HSLA) steels. *Mater Sci Eng A* 760:125–133. <https://doi.org/10.1016/j.msea.2019.05.120>
- [24] Jiang Q, Bertolo VM, Popovich VA, et al (2021) Relating matrix stress to local stress on a hard microstructural inclusion for understanding cleavage fracture in high strength steel. *Int J Fract* 1–34. <https://doi.org/10.1007/s10704-021-00587-y>
- [25] CEN (2019) NEN-EN 10025-6: Hot rolled products of structural steels—Part 6: technical delivery conditions for flat products of high yield strength structural steels in the quenched and tempered condition
- [26] ASTM International (2016) ASTM E1245-03: standard practice for determining the inclusion or second-phase constituent content of metals by automatic image analysis. <https://doi.org/10.1520/E1245-03R08.2>
- [27] Hesamodin Talebi S, Ghasemi-Nanasa H, Jahazi M, Melkonyan H (2017) In situ study of phase transformations during non-isothermal tempering of bainitic and martensitic microstructures. *Metals (Basel)* 7:1–13. <https://doi.org/10.3390/met7090346>
- [28] Sente Software JMatPro® API
- [29] Cayron C (2007) ARPGE: a computer program to automatically reconstruct the parent grains from electron backscatter diffraction data. *J Appl Crystallogr* 40:1183–1188. <https://doi.org/10.1107/S0021889807048777>
- [30] ASTM International (2012) ASTM E112-13 Standard test methods for determining average grain size. *ASTM Int* 1–27



- [31] Rodríguez R, Gutierrez I (2003) Correlation between nanoindentation and tensile properties Influence of the indentation size effect. *Mater Sci Eng* 361:377–384. [https://doi.org/10.1016/S0921-5093\(03\)00563-X](https://doi.org/10.1016/S0921-5093(03)00563-X)
- [32] Oliver WC, Pharr GM (1992) An improved technique for determining hardness and elastic modulus using load and displacement sensing indentation experiments. *J Mater Res* 7:1564–1583. <https://doi.org/10.1557/JMR.1992.1564>
- [33] ISO (2018) ISO 12135: metallic materials—unified method of test for the determination of quasistatic fracture toughness. 2016
- [34] Canale LCF, Vatavuk J, Totten GE (2014) 12.02—Introduction to steel heat treatment. In: Hashmi S, Batalha GF, Van Tyne CJ, Yilbas B (eds) *Comprehensive materials processing*. Elsevier, Oxford, pp 3–37
- [35] Feng R, Li S, Zhu X, Ao Q (2015) Microstructural characterization and formation mechanism of abnormal segregation band of hot rolled ferrite/pearlite steel. *J Alloys Compd* 646:787–793. <https://doi.org/10.1016/j.jallcom.2015.05.128>
- [36] Guo F, Liu W, Wang X et al (2019) Controlling variability in mechanical properties of plates by reducing centerline segregation to meet strain-based design of pipeline steel. *Metals (Basel)* 9:1–11. <https://doi.org/10.3390/met9070749>
- [37] Suikkanen PP, Ristola A, Hirvi AM et al (2013) Effects of carbon content and cooling path on the microstructure and properties of TRIP-aided ultra-high strength steels. *ISIJ Int* 53:337–346. <https://doi.org/10.2355/isijinternational.53.337>
- [38] van Bohemen SMC (2012) Bainite and martensite start temperature calculated with exponential carbon dependence. *Mater Sci Technol* 28:487–495. <https://doi.org/10.1179/1743284711Y.0000000097>
- [39] Takayama N, Miyamoto G, Furuhashi T (2012) Effects of transformation temperature on variant pairing of bainitic ferrite in low carbon steel. *Acta Mater* 60:2387–2396. <https://doi.org/10.1016/j.actamat.2011.12.018>
- [40] Papaefthymiou S, Bouzouni M, Petrov RH (2018) Study of carbide dissolution and austenite formation during ultra-fast heating in medium carbon chromium molybdenum steel. *Metals (Basel)* 8:1–17. <https://doi.org/10.3390/met8080646>
- [41] Tsuchiyama T, Natori M, Nakada N, Takaki S (2010) Conditions for grain boundary bulging during tempering of lath martensite in ultra-low carbon steel. *ISIJ Int* 50:771–773. <https://doi.org/10.2355/isijinternational.50.771>
- [42] Bhadeshia H, Honeycombe R (2017) *Steels: microstructure and properties*, 4th edn. Butterworth-Heinemann
- [43] Nagode A, Resnik A, Vertnik R et al (2017) The development of a banded microstructure in S355J2 steel bar. *Kov Mater* 55:51–56. <https://doi.org/10.4149/km2017>
- [44] Choi W, Matsuura H, Tsukihashi F (2013) Effect of nitrogen on the formation and evolution of non-metallic inclusions in Fe–Al–Ti–N alloy. *ISIJ Int* 53:2007–2012. <https://doi.org/10.2355/isijinternational.53.2007>
- [45] Subramanian SV, Xiaoping M, Wenjin N, Xiaobing Z (2015) Application of nano-scale precipitate engineering of TiN-NbC composite in 32 mm K60-E2 grade plate rolling. In: *HSLA steels 2015, microalloying 2015 & offshore engineering steels*. pp 211–221
- [46] da Costa e Silva ALV (2019) The effects of non-metallic inclusions on properties relevant to the performance of steel in structural and mechanical applications. *J Mater Res Technol*. <https://doi.org/10.1016/j.jmrt.2019.01.009>
- [47] Mandal SK (2015) *Steel metallurgy—properties, specifications, applications*. McGraw-Hill
- [48] Morris Jr JW (2001) The influence of grain size on the mechanical properties of steel. In: *International symposium on ultrafine grained steels*. Fukuoka
- [49] Morris JW Jr, Kinney C, Pytlewski K, Adachi Y (2013) Microstructure and cleavage in lath martensitic steels. *Sci Technol Adv Mater* 14:1–9. <https://doi.org/10.1088/1468-6996/14/1/014208>
- [50] Prawoto Y, Jasmawati N, Sumeru K (2012) Effect of prior austenite grain size on the morphology and mechanical properties of martensite in medium carbon steel. *J Mater Sci Technol* 28:461–466. [https://doi.org/10.1016/S1005-0302\(12\)60083-8](https://doi.org/10.1016/S1005-0302(12)60083-8)
- [51] Rancel L, Gómez M, Medina SF, Gutierrez I (2011) Measurement of bainite packet size and its influence on cleavage fracture in a medium carbon bainitic steel. *Mater Sci Eng A* 530:21–27. <https://doi.org/10.1016/j.msea.2011.09.001>
- [52] Wang C, Wang M, Shi J et al (2007) Effect of microstructure refinement on the strength and toughness of low alloy martensitic steel. *J Mater Sci Technol* 23:659–664
- [53] Wang BIN, Wang Z, Wang B-X et al (2015) The relationship between microstructural evolution and mechanical properties of heavy plate of low-Mn steel during ultra fast cooling. *Metall Mater Trans A* 46A:2834–2843. <https://doi.org/10.1007/s11661-015-2933-1>
- [54] Cahn JW (1962) The impurity-drag effect in grain boundary motion. *Acta Metall* 10:789–798. [https://doi.org/10.1016/0001-6160\(62\)90092-5](https://doi.org/10.1016/0001-6160(62)90092-5)
- [55] Reiter J, Bernhard C, Presslinger H (2008) Austenite grain size in the continuous casting process: metallographic methods and evaluation. *Mater Charact* 59:737–746. <https://doi.org/10.1016/j.matchar.2007.06.003>
- [56] Li H, Gao S, Tian Y et al (2015) Influence of tempering on mechanical properties of ferrite and martensite dual phase steel. In: *International conference on martensitic transformations, ICOMAT-2014*. pp S667–S671. <https://doi.org/10.1016/j.matpr.2015.07.372>

- [57] Chen JH, Cao R (2015) Micromechanism of cleavage fracture of metals. Butterworth-Heinemann, Boston
- [58] Griffith AA (1920) The phenomena of rupture and flow in solids. *Philos Trans R Soc A Math Phys Eng Sci C*:163–198
- [59] Ghosh A, Ray A, Chakrabarti D, Davis CL (2013) Cleavage initiation in steel: competition between large grains and large

particles. *Mater Sci Eng A* 561:126–135. <https://doi.org/10.1016/j.msea.2012.11.019>

**Publisher's Note** Springer Nature remains neutral with regard to jurisdictional claims in published maps and institutional affiliations.